

Department of Chemical Engineering and Chemistry SPI Research Group

A Multi-Physics Model of Hydrogen Permeation through Pd-Ag Membranes

Quantifying Ammonia Inhibition in Catalytic Membrane Reactors

I. A. Badmus

Supervisors:

Prof. dr. ir. M. van Sint Annaland
Prof. dr. ir. Fausto Gallucci
Dr. Valentina Cechetto
Msc. Roberto Fiorillo

Master Thesis

Eindhoven, August 2025

Abstract

Ammonia is a promising carrier for storing and transporting hydrogen, but its efficient decomposition into high-purity hydrogen remains a challenge. Catalytic membrane reactors (CMRs) equipped with palladium-based membranes offer an elegant solution by integrating reaction and separation, yet their performance is critically influenced by complex transport phenomena and potential inhibition by ammonia.

This thesis develops and rigorously validates a predictive, multi-physics model for hydrogen permeation through a supported Pd-Ag membrane to de-risk its application in ammonia cracking environments. The model is constructed incrementally, coupling external gas-film mass transfer, a modified Sieverts' law for the dense Pd-Ag layer, and a Dusty Gas Model for the porous support. A sequential validation strategy was employed using permeation datasets from Cechetto et al. (2021). First, using non-inhibiting H_2/N_2 mixtures, a robust baseline model was established that demonstrated excellent agreement with experimental data ($R^2 \approx 0.97$, MAPE $\approx 3.2\%$).

This analysis revealed that hydrogen transport is co-limited by permeation through the dense metal and external mass transfer resistance, with the support playing a minor role. When applied to $\rm H_2/NH_3$ mixtures, the baseline model systematically overpredicted the hydrogen flux, providing clear evidence of inhibition. The introduction of a physically-grounded Langmuir-Hinshelwood site-blocking term successfully eliminated this bias. The fitting procedure quantified ammonia as a weak, reversible inhibitor at typical operating temperatures (> 400 °C), with a fitted enthalpy of adsorption ($\Delta H_{\rm ads} \approx -40~{\rm kJ/mol}$) consistent with weak molecular chemisorption. Furthermore, the validated mechanistic model was compared with a permeation model based on modified Sieverts' law, demonstrating consistently higher $\rm H_2$ recovery of approximately 6–12 percentage points across the studied temperature range.

Ultimately, this work delivers a validated, physics-based tool that not only accurately describes the permeation process but also provides crucial parameters for the design and optimization of ammonia decomposition membrane reactors. The findings confirm the viability of Pd-Ag membranes for this application by quantitatively demonstrating that ammonia inhibition is a manageable phenomenon, thereby advancing a key technology for the hydrogen economy.

Acknowledgements

This Master's thesis represents the culmination of a challenging yet deeply rewarding journey. It is a work that would not have been possible without the collective guidance, support, and encouragement of many remarkable individuals, and it is with the sincerest gratitude that I acknowledge their contributions.

First and foremost, I wish to express my profound appreciation to my supervisors, Professor Martin van Sint Annaland and Professor Fausto Gallucci. Their intellectual generosity, insightful guidance, and unwavering belief in my potential formed the bedrock of this project. They consistently challenged me to think more critically, pushed me to refine my ideas, and provided the steady mentorship that was instrumental in bringing this work to fruition.

My sincere thanks extend to Dr. Jurriaan Boon for his invaluable support during the formative stages of this research; his early input was crucial in setting a strong foundation for the entire project. I am also incredibly thankful for the motivation from my colleagues. I owe a special debt of gratitude to my direct supervisor, Roberto, for his constant availability and steadfast support, and to Valentina, whose generously shared experimental datasets gave this thesis greater depth and meaning. Their friendship transformed daily challenges into manageable hurdles and made this academic pursuit all the more enjoyable.

I am deeply grateful to the HySET program for awarding me the scholarship that made this fantastic journey possible. This opportunity was far more than financial; it was a vote of confidence that opened the door to an enriching academic world. As the saying goes, "if I have seen further, it is by standing on the shoulders of giants," and I am indebted to the many researchers and thinkers whose work paved the way for my own.

Finally, I owe my deepest and most personal thanks to my family. Embarking on this journey required the difficult step of leaving them behind. Their immense sacrifices, endless encouragement, and unwavering belief in me have been my greatest source of strength. This achievement is as much theirs as it is mine, and for their unconditional love and support, I am eternally grateful.

Contents

Co	Contents			
Lis	st of F	igures		хi
Lis	st of T	ables		xiii
1	Intr	oductio	on Control of the Con	1
	1.1	Resea	rch Objectives and Approach	3
2	The	ory		5
	2.1	Ammo	onia Decomposition in Different Reactor Configurations	5
		2.1.1	Thermodynamic Fundamentals and Reaction Characteristics	5
		2.1.2	Reaction Kinetics and Mechanistic Pathways	6
		2.1.3	Catalyst Families for Ammonia Decomposition	6
		2.1.4	Catalytic Membrane Reactors	7
	2.2	Hydro	gen Permeation in Palladium-Based Membranes	9
		2.2.1	Material Properties and Operating Window	9
		2.2.2	The Multi-Step Solution-Diffusion Mechanism	9
		2.2.3	The Ideal Model: Diffusion-Limited Transport	10
		2.2.4	Modeling Deviations from Ideality: Analysis of Transport Resistances	12
	2.3		nce of Operating Parameters and System Design	14
	2.4		Validation and Experimental Correlation	14
		2.4.1	Coefficient of Determination (R^2)	14
		2.4.2	Mean Absolute Percentage Error (MAPE)	15
3	Mod	lelling F	Framework Tramework	17
	3.1	Scope	and Assumptions	17
	3.2	Geom	etry and Operating Envelope	18
	3.3	Gover	ning Equations	19
		3.3.1	External Gas-Film Mass Transfer	20
		3.3.2	Permeation Through Dense Pd-Ag	21
		3.3.3	Porous Support Transport	21
		3.3.4	Film-Membrane Coupling and Concentration Polarization	22

		3.3.5	Ammonia Inhibition	22
	3.4	Axial M	laterial Balance	23
	3.5	Numer	rical Solution	24
	3.6	Membi	rane Reactor Model	26
4			Discussion	27
	4.1		eter Estimation Strategy	27
	4.2		ne Model Validation: H_2/N_2 Permeation	27
		4.2.1	Dataset and Goodness of Fit	27
		4.2.2	Transport Resistance Analysis	28
		4.2.3	Robustness to Sherwood Correlation	30
	4.3	Modeli	ng Ammonia Inhibition Effects	32
		4.3.1	Baseline Model Performance on H_2/NH_3 Mixtures	32
		4.3.2	Fitting a Langmuir-Hinshelwood Inhibition Model	32
	4.4	Model	Selection and Robustness Analysis	35
		4.4.1	Temperature Dependence of Inhibition	35
		4.4.2	Independent Per-Temperature Fits and Van't Hoff Analysis	35
	4.5	Membi	rane Reactor Model: Comparing Simplified and Mechanistic Permeation Models	36
		4.5.1	Reactor Geometry and Operating Conditions	36
		4.5.2	H ₂ Recovery	36
		4.5.3	NH ₃ Conversion	38
		4.5.4	Permeate H ₂ Purity	38
		4.5.5	Permeate H ₂ Molar Flow	38
		4.5.6	Summary of Model Comparison	39
5	Con	rlusione	s and Outlook	43
•	5.1		isions	43
	5.2		mendations	44
	5.2	5.2.1	Experimental Validation and Parametric Expansion	44
		5.2.2	Model Refinement and Extension	44
		5.2.3	Application and System-Level Integration	44
	5.3		Outlook	44
Ap	pend	IX		50
A	Prop	_	orrelations and Supporting Derivations	51
	A.1	Mixture	e-Property Relations	51
		A.1.1	Component Viscosity	51
		A.1.2	Mixture Viscosity	51
		A.1.3	Binary Diffusion Coefficients	52
		A.1.4	Effective Mixture Diffusivity	52
		A.1.5	Viscosity Coefficients	52
		A.1.6	Component Properties	52

В	Dust	ty Gas Model Equations			
	B.1	General Form with Viscous Contribution	55		
	B.2	Negligible Pressure Drop (No Viscous Contribution)	55		
	B.3	Rewritten Form	55		
	B.4	Three-Component System	56		
	B.5	Two-Component Dusty Gas Model	56		
	B.6	Simplified Expressions	56		
	B.7	Flux Expression	56		
	B.8	Relation	56		
	B.9	One-Component Dusty Gas Model	57		
	B.10	Parameter Definitions	57		
C	Ехре	erimental Permeation Data	59		
	C.1	Experimental Permeation Data	59		
		C.1.1 H ₂ /N ₂ System	59		
		C.1.2 H ₂ /NH ₃ System	60		
		C.1.3 Experimental Conditions	60		

List of Figures

1.1	Hydrogen densities of different carriers demonstrating the high density associated with ammonia [8]	2
1.2	Process efficiency of CMR compared to conventional ammonia crackers[12]	3
2.1	Schematic pathway for catalytic NH ₃ decomposition (dehydrogenation sequence and recombinative desorption), adapted from [7]	6
2.2	Packed-bed membrane reactor: shell (a) and tube (b) configurations.[11]	7
2.3	Schematic representation of a conventional system (a) and a membrane reactor-based system (b) for hydrogen production via ammonia decomposition [11].	8
2.4	The sequence of transport steps for hydrogen permeation through a supported palladium membrane [13]	10
2.5	Solution-Diffusion mechanism	11
3.1	Schematic of the transport layers: external gas film, Pd–Ag layer, and porous alumina support. Adapted from Boon et al. (2015) [17].	18
3.2	Axial discretization of the membrane, modeled as annular unit cells with axial flow and radial permeation, as adapted from [16]	24
3.3	Flowchart of the nested iteration strategy for hydrogen flux calculation through Pd–Ag membranes	25
4.1	Hydrogen permeability of various Pd–metal binary alloy membranes $\operatorname{Pd}_x \operatorname{M}_{(100-x)}$ (where $(100-x)$ represents the atomic concentration of the solute metal) at 873 K, with the metal M's group in the Periodic Table of Elements indicated. The letter "B" in the figure represents a Group in the Periodic Table of Elements, and the preceding Roman numeral assigned before "B" follows the American Group labelling scheme. Readapted	
	from [37]	28
4.2	Parity plot for the baseline H_2/N_2 permeation model, showing excellent agreement between predicted and experimental flow rates. (R^2 =0.969, MAPE=3.31)	29
4.3	Partitioning of transport resistances under representative high-flux conditions. The external gas film and dense Pd–Ag layer dominate, while the porous support is negligible.	30
4.4	Axial evolution of hydrogen recovery and capacity ratio, showing increasing polarization toward the outlet.	31

Simulated hydrogen partial pressure ladders across the membrane at different axial	
positions, illustrating the buildup of concentration polarization.	31
Parity plot for H_2/NH_3 mixture - NO inhibition, showing excellent agreement between	
predicted and experimental flow rates. (R^2 =0.829, MAPE=8.86)	33
Baseline H_2/NH_3 Residuals versus feed x_{NH_3} . Systematic positive bias grows with NH_3 ,	
indicating missing inhibition physics	33
Comparison of parity plots for H_2/NH_3 mixtures: the baseline model (blue), the temperature of the comparison of parity plots for H_2/NH_3 mixtures:	<u> </u>
independent inhibition model (orange), and the full van't Hoff model (green)	34
Residuals versus feed $x_{ m NH_3}$ for all three models. Incorporation of the inhibition term	
(orange and green) removes the systematic bias present in the baseline model (blue)	34
$\label{thm:constant} \textbf{Van't Hoff plot derived from fitting the adsorption constant} \textit{K} \textbf{ independently at each}$	
temperature. The shallow slope indicates a weak temperature dependence	36
Comparative performance plots of the simplified PBMR permeation law (orange) and the	
validated mechanistic model (blue). Panels show: H ₂ recovery (top left), NH ₃ conversion	
(top right), permeate H_2 purity (bottom left), and permeate H_2 molar flow (bottom right).	37
Ammonia conversion profile along the reactor	37
(Top)Temperature profile along the reactor, showing inlet temperatures (350–450°C),	
(Bottom) H ₂ concentration, peaking due to NH ₃ decomposition, then declining in the	
membrane zone	40
(Bottom)NH ₃ and H ₂ mole fractions; membrane zone accelerates H ₂ production and	
removal	41
	Parity plot for H_2/NH_3 mixture - NO inhibition, showing excellent agreement between predicted and experimental flow rates. $(R^2$ =0.829, MAPE=8.86)

List of Tables

2.1	Representative catalyst families for NH ₃ decomposition. Illustrative performance envelopes for ammonia decomposition in conventional packed	7
	beds (PBR) and catalytic membrane reactors (CMR). Values indicate typical ranges in the literature.	9
2.3	Qualitative comparison of H ₂ -separation membrane classes	9
3.1	Governing equations for hydrogen transport and ammonia inhibition.	20
3.2	Comparison of Reactor Model and Validated Permeation Model Features	26
4.1	Detailed mass transfer analysis and sensitivity to support morphology	30
4.2	Summary of fit performance for different Sherwood number correlations. [16, 38]	31
4.3	Ammonia Adsorption Enthalpies on Pd-Based Surfaces	35
4.4	Geometric Parameters of the Packed Bed Membrane Reactor (PBMR)	38
4.5	Comparison of simplified PBMR law vs. validated mechanistic permeation model across	
	performance metrics	39
A.1	Viscosity correlation coefficients for individual species	52
A.2	Component properties used in transport property correlations	52
C.1	Experimental hydrogen permeation data for H ₂ /N ₂ mixtures	59
C 2		60

Nomenclature

Symbol	Description	Units	
Roman Symbols			
A_i	Area of axial slice <i>i</i>	m^2	
B_0	Viscous flow permeability parameter (DGM)	m^2	
C	Concentration of dissolved hydrogen	$ m molm^{-3}$	
C_{bulk}	Bulk molar concentration	$ m mol~m^{-3}$	
c_{tot}	Total molar concentration	$\mathrm{mol}\mathrm{m}^{-3}$	
D	Diffusion coefficient	$\mathrm{m}^2\mathrm{s}^{-1}$	
$D_{ij,eff}$	Effective binary molecular diffusivity	$\mathrm{m}^2\mathrm{s}^{-1}$	
$D_{iK,eff}$	Effective Knudsen diffusivity	$\mathrm{m}^2\mathrm{s}^{-1}$	
$D_{H_2,mix}$	Diffusion coefficient of H ₂ in mixture	$\mathrm{m}^2\mathrm{s}^{-1}$	
d	Characteristic length (e.g., diameter)	m	
d_h	Hydraulic diameter	m	
d_p	Average pore diameter	m	
E_A, E_p	Activation energy for permeation	${\sf J}{\sf mol}^{-1}$	
$F^{(i)}$	Molar flow rate at axial slice i	$ m mols^{-1}$	
f_{inh}	Inhibition factor	_	
J	Molar flux	$\mathrm{mol}\mathrm{m}^{-2}\mathrm{s}^{-1}$	
$j_{\sf actual}$	Actual permeation flux	$\mathrm{mol}\mathrm{m}^{-2}\mathrm{s}^{-1}$	
K_i Adsorption equilibrium constant for species i		Pa^{-1}	
K_0	Pre-exponential factor for inhibition constant	Pa^{-m}	
K_S	Sieverts' constant	$\mathrm{mol}\mathrm{m}^{-3}\mathrm{Pa}^{-0.5}$	
k_c, k_g, k_m	Mass transfer coefficient	${\sf m}{\sf s}^{-1}$	
L	Membrane thickness	m	
M_i	Molar mass of component i	${\sf kg}{\sf mol}^{-1}$	
m	Pressure exponent for inhibition	_	
N_i	Molar flux of component i (DGM)	$ m molm^{-2}s^{-1}$	
n	Pressure exponent (Sieverts' Law)	_	
'n	Molar flow rate	$\mathrm{mol}\mathrm{s}^{-1}$	
P	Total pressure	Pa	
P_i	Partial pressure of species <i>i</i>	Pa	

Symbol	Description	Units
P_H	Hydrogen permeability	$\operatorname{mol}\operatorname{m}^{-1}\operatorname{s}^{-1}\operatorname{Pa}^{-n}$
P_0	Pre-exponential factor for permeability	$\operatorname{mol}\operatorname{m}^{-1}\operatorname{s}^{-1}\operatorname{Pa}^{-n}$
$Pe_0(T)$	Temperature-dependent permeance	$\operatorname{mol}\operatorname{m}^{-2}\operatorname{s}^{-1}\operatorname{Pa}^{-n}$
R	Universal gas constant	$\mathrm{J}\mathrm{mol}^{-1}\mathrm{K}^{-1}$
r_{memb}	Membrane radius	m
S_i	Sutherland constant for component i	K
T	Absolute temperature	K
и	Fluid velocity	$\mathrm{m}\mathrm{s}^{-1}$
V_A	Molecular diffusion volume	$\mathrm{cm}^3\mathrm{mol}^{-1}$
\dot{V}	Volumetric flow rate	$\mathrm{m}^3\mathrm{s}^{-1}$
x	Spatial coordinate	m
x_i, y_i	Mole fraction of component <i>i</i>	-
Z	Axial transport coordinate	m
Greek Symb	ols	
α	Correction factor for mass transfer coefficient	-
ΔH_{ads}	Enthalpy of adsorption	$Jmol^{-1}$
ΔH_r°	Standard enthalpy of reaction	$Jmol^{-1}$
δ	Boundary layer thickness	m
ϵ	Porosity	_
Θ_i	Fractional surface coverage of species <i>i</i>	_
μ_i	Viscosity of component <i>i</i>	Pa s
μ_{mix}	Mixture viscosity	Pa s
ρ	Density	${ m kg}{ m m}^{-3}$
τ	Tortuosity	-
Φ	Capacity ratio	-
ϕ_{ij}	Wilke's mixing rule interaction parameter	-
Dimensionle	ess Numbers	
Da _{MT}	Damköhler number for mass transfer	-
Gz	Graetz number	-
Re	Reynolds number	-
Sc	Schmidt number	-
Sh	Sherwood number	-
Subscripts a	nd Superscripts	
bulk	Bulk fluid phase property	
eff	Effective property in porous medium	
feed	Feed side property	
int	Internal interface property	
memb	Membrane surface property	
perm	Permeate side property	

Symbol	Description	Units	
surf	Surface property		
Acronyms			
CMR	Catalytic Membrane Reactor		
CP	Concentration Polarization		
DGM	Dusty Gas Model		
HRF	RF Hydrogen Recovery Fraction		
MAPE	Mean Absolute Percentage Error		
MSE	Mean Squared Error		
PBR	Packed Bed Reactor		
TEA	Techno-Economic Analysis		

Chapter 1

Introduction

The increasing global demand for sustainable and clean energy has placed hydrogen as a potential clean energy vector in the current energy transition drive [1, 2, 3]. Its potential to meet a substantial part of the world's energy needs by 2050 highlights its significance in global decarbonisation efforts [3]. Its flexibility to be used both as an energy carrier and as a feedstock allows for applications across various sectors, especially in areas that are hard to decarbonise through other means, such as heavy industries and long-distance transport [2]. Although the demand for hydrogen has been increasing recently, most of its use is in the refining and chemical sectors, especially for the production of ammonia, which is predominantly produced through catalytic steam methane reforming (SMR) of fossil fuels, particularly natural gas [4]. However, the environmental footprint of these traditional methods underscores the need for cleaner alternatives. Furthermore, developing efficient and less expensive production and separation processes would enhance hydrogen's potential as a clean hydrogen vector.

For hydrogen production, there has been a huge effort placed on renewable-powered electrolysis of water as a cleaner alternative, however, its widespread adoption is hindered by high costs and significant energy losses [5]. Besides production, there is also the challenge of hydrogen storage and transport. Though hydrogen has a high energy density, its low volumetric energy density makes its storage complicated [6, 7]. To address this complication, various methods, including compression, liquefaction, and storage in metal hydrides, have been explored, but hydrogen's low molecular weight makes it prone to diffusing through metals, causing embrittlement [6].

To comprehensively address the issues stated earlier, different 'hydrogen carriers' are being explored [8]. Ammonia, because of its high hydrogen content (17.8 percent by weight) and its ease of liquefaction at low pressures, has emerged as a promising hydrogen carrier [9]. Figure 1.1 compares the hydrogen density of ammonia to other selected carriers. High-purity hydrogen can be produced from ammonia decomposition (or cracking), and conventional ammonia crackers typically require high temperatures for complete conversion, making it also highly energy-intensive and a major contributor to global CO_2 emissions [10].

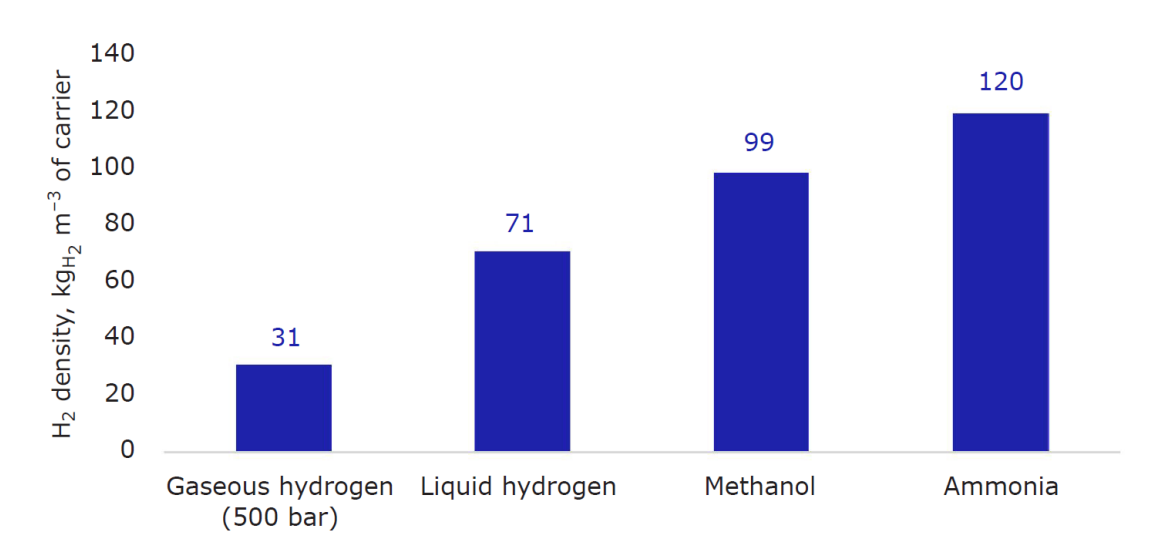


Figure 1.1: Hydrogen densities of different carriers demonstrating the high density associated with ammonia [8]

Despite the advantages of conventional ammonia decomposition, there are still some challenges. These include its requirement of high temperature, as mentioned earlier, and the need for efficient catalysts to achieve complete conversion [7]. Also, unconverted ammonia can find its way to the hydrogen product stream, thus creating a potential for poisoning in high-purity applications, such as in fuel cells. This necessitates an efficient and cost-effective separation technology [11].

Membrane technologies play an important role in enhancing the efficiency and performance of ammonia decomposition technologies by selectively separating hydrogen from the reaction products, thus achieving high hydrogen purity [7]. Although various membranes are currently available, palladium-based membranes stand out for their exceptional selectivity and permeability towards hydrogen while being virtually impermeable to other gases like nitrogen (N_2) and ammonia [11]. It has been demonstrated that with their integration into catalytic membrane reactors (CMR), thermodynamic equilibrium limitations were surpassed, and there is a notable improvement in process efficiency, as shown in Figure 1.2 [7, 11].

These membranes typically consist of a thin, dense layer of palladium or a palladium alloy deposited onto a porous support material. The porous support, often ceramic or metallic, provides the necessary mechanical strength to the thin selective layer, allowing it to withstand significant pressure differentials and high temperatures. The advantages of Pd-based membranes are numerous, including near-infinite selectivity for hydrogen over N_2 and NH_3 , high hydrogen permeability, and the capability to produce fuel-cell grade hydrogen (e.g., >99.998% purity) without requiring extensive downstream purification units like pressure swing adsorption (PSA) systems [7, 11, 12].

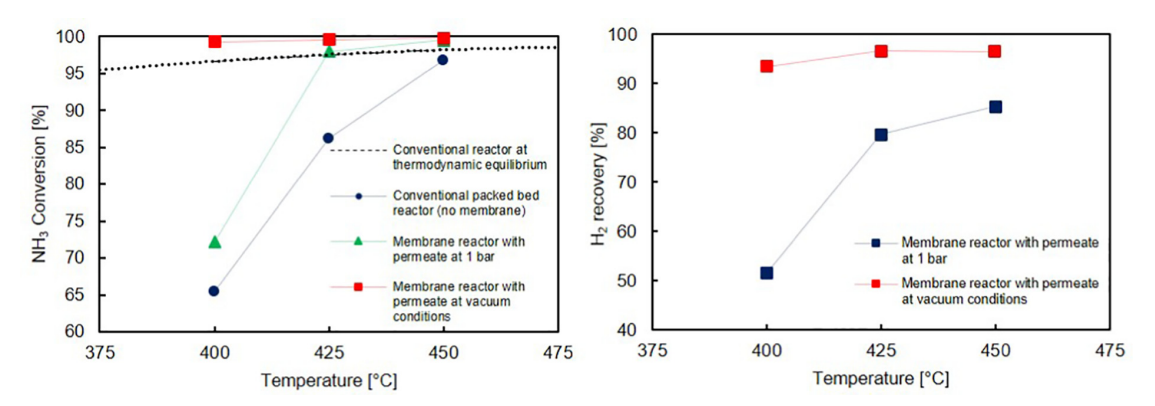


Figure 1.2: Process efficiency of CMR compared to conventional ammonia crackers[12]

The advantages of palladium-based membranes are evident, however, they face challenges related to poisoning by impurities, long-term stability, and scalability [13]. To address these issues, there is an ongoing research effort focused on strategies that include alloying (e.g., Pd-Ag membranes), advanced support materials, and novel reactor designs [14, 11]. Furthermore, optimising the design and operation of these membranes requires accurate modelling of the mass transport process of hydrogen.

The overall rate of hydrogen permeation through a supported palladium membrane is a complex function of multiple interacting phenomena [13]. These include mass transfer resistances in the gas phases on both sides of the membrane, the kinetics of hydrogen interaction with the palladium surface (adsorption, dissociation, solution), diffusion through the palladium lattice, transport through the porous support structure, and the influence of operating conditions such as temperature, pressure, and the presence of other gaseous species [15]. The presence of nitrogen and unconverted ammonia from the ammonia cracking reaction can particularly influence hydrogen flux through concentration polarization effects and competitive adsorption on the palladium surface respectively [16]. Accurate and detailed mathematical models that can describe these phenomena are indispensable for the rational design, optimization, and scale-up of ammonia cracking membrane reactors [15]. Such models allow for the prediction of membrane performance under various operating conditions, identification of rate-limiting steps, and exploration of strategies to enhance hydrogen recovery and purity [17].

1.1 Research Objectives and Approach

The primary objective of this research is to develop and validate a predictive, physics-based model for hydrogen transport through composite palladium-based membranes, capturing the layer-by-layer transport phenomena within a catalytic membrane reactor (CMR) for ammonia decomposition. This framework will enable quantification of individual resistance contributions, assessment of ammonia inhibition, and benchmarking against a simpler, conventional model. To achieve this, the following objectives were defined:

- 1. Develop a one-dimensional (1D) permeation model.
- 2. Validate the model in a sequential framework by systematically isolating and quantifying:

- (a) External mass transfer resistance using binary H_2/N_2 mixture data.
- (b) The inhibitory effect of ammonia via a Langmuir-type adsorption term, validated against H_2/NH_3 mixture data.
- 3. Integrate the fully validated permeation model with a comprehensive reactor model to support system design studies and high-level process optimization.
- 4. Compare the predictive accuracy of the comprehensive model with a lumped permeation model based on modified Sieverts' Law, quantifying the benefits of the more detailed approach.

Chapter 2

Theory

This chapter provides the theoretical basis for hydrogen permeation through supported palladium membranes in ammonia decomposition environments. It first outlines the thermodynamics and catalysis of ammonia decomposition, contrasts conventional and catalytic membrane reactor concepts, and introduces palladium membranes as selective separation media. The discussion then develops hydrogen transport models from ideal to non-ideal regimes, culminating in a resistance-in-series framework that motivates the integrated modeling approach of this work.

2.1 Ammonia Decomposition in Different Reactor Configurations

2.1.1 Thermodynamic Fundamentals and Reaction Characteristics

The decomposition of ammonia is an endothermic process in which ammonia molecules (NH_3) dissociate into nitrogen (N_2) and hydrogen (N_2) in the presence of heat, typically promoted by heterogeneous catalysts. The reaction is expressed as

$$NH_3 \Longrightarrow \frac{1}{2}N_2 + \frac{3}{2}H_2, \qquad \Delta H_r^{\circ}(298 \text{ K}) \approx +46 \text{ kJ/mol.}$$
 (2.1)

The positive enthalpy indicates that significant energy input is required for reaction progress. Consequently, the decomposition of NH_3 becomes thermodynamically favorable only at elevated temperatures, with appreciable equilibrium conversion achieved above approximately 450 K (177°C). At atmospheric pressure, equilibrium conversion exceeds 99 % at temperatures above 700 K (427°C) [7, 18]. Pressure effects follow Le Chatelier's principle: increased pressure shifts equilibrium toward ammonia formation, such that complete conversion at 5 bar requires temperatures in excess of (600°C), thereby incurring substantial energy penalties in conventional reactors.

The reaction is also accompanied by molar expansion (2 mol reactants \rightarrow 4 mol products), favoring low-pressure operation from both thermodynamic and kinetic perspectives. This feature becomes particularly advantageous in membrane reactor configurations, where selective hydrogen removal lowers the local $\rm H_2$ partial pressure and thereby drives equilibrium conversion at reduced bulk temperatures.

In industrial practice, ammonia decomposition is typically conducted in a high-temperature, low-

pressure reactor followed by downstream separation units to recover N_2 and unreacted N_3 while producing a hydrogen-rich stream. Process intensification strategies generally focus on two levers: (i) the development of highly active catalytic systems, and (ii) the selective removal of hydrogen during reaction to shift equilibrium conversion [7, 18].

2.1.2 Reaction Kinetics and Mechanistic Pathways

Ammonia decomposition is a surface-catalyzed process with apparent activation energies typically ranging from $100\,\mathrm{kJ\,mol^{-1}}$ to $250\,\mathrm{kJ\,mol^{-1}}$ depending on catalyst formulation and operating conditions. The widely accepted mechanistic pathway involves adsorption of ammonia, followed by sequential N-H bond cleavage (NH $_3$ · \longrightarrow NH $_2$ · \longrightarrow NH· \longrightarrow N·), recombination of adsorbed nitrogen to form N $_2$, and recombinative desorption of H $_2$ as depicted in Figure 2.1.

The kinetically limiting step is most often associated with N–N bond formation and N_2 desorption at temperatures below $\sim\!1000\,\mathrm{K}$, whereas ammonia adsorption can become rate-limiting at higher temperatures. This duality highlights the strong sensitivity of decomposition rates to catalyst composition and operating window. Ruthenium-based catalysts represent the benchmark materials due to their optimal Ru–N binding energies, which lower the activation barrier for nitrogen recombination and enable high activity at temperatures as low as 400°C .

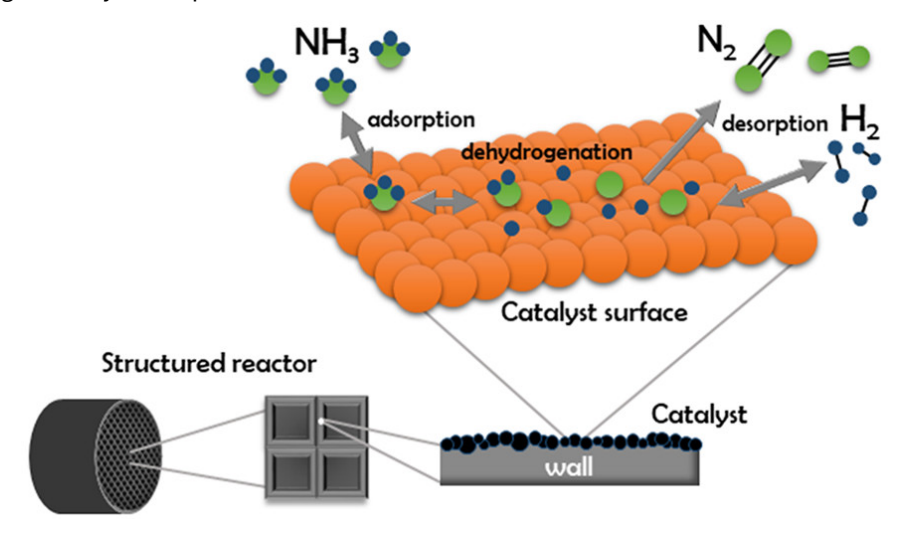


Figure 2.1: Schematic pathway for catalytic NH₃ decomposition (dehydrogenation sequence and recombinative desorption), adapted from [7].

2.1.3 Catalyst Families for Ammonia Decomposition

Considerable research has been devoted to the identification of catalyst families capable of achieving high ammonia conversion at reduced temperatures and energy inputs. Representative classes are summarized in Table 2.1.

Among these, ruthenium-based catalysts deliver the highest intrinsic activity, whereas promoted Ni systems represent the most cost-effective alternatives and have seen substantial improvements in

Catalyst family	Typical T for high $X_{ m NH_3}$	Notes		
Ru/oxide (e.g., Ru/Y, Ru/MgO, Ru/CeO ₂)	~380-500 °C	Highest intrinsic activity; strong metal–support and basicity effects; lower T achievable with optimized sites [7, 18].		
Ni (promoted; e.g., Ni/La–Al, Ni/Ca–Al, alkali- doped)	~500-650 °C	Cost-effective; improved dispersion/basicity mitigate higher T ; substantial progress in the past decade [7, 18].		
Fe, Co, nitrides/carbides	≳550-700 °C	Alternative non-noble systems; stability and poisoning sensitivity vary [7, 18].		

Table 2.1: Representative catalyst families for NH₃ decomposition.

dispersion and basicity over the past decade. Non-noble metal catalysts (Fe, Co) and transition-metal nitrides/carbides offer promising stability under certain conditions, though challenges with poisoning and higher operational temperatures remain.

2.1.4 Catalytic Membrane Reactors

Conventional packed-bed reactors (PBRs) for ammonia decomposition are limited by thermodynamic equilibrium, requiring elevated temperatures to achieve high conversion. The resulting effluent contains a mixture of N_2 , H_2 , and unreacted NH_3 , which necessitates downstream separation to obtain high-purity hydrogen. In contrast, catalytic membrane reactors (CMRs) integrate reaction and separation within a single unit. A hydrogen-selective membrane, typically based on Pd alloys, continuously removes H_2 as it is generated, thereby shifting equilibrium toward products in accordance with Le Châtelier's principle and simultaneously delivering a purified hydrogen stream [11, 12]. A comparison between PBRs and CMRs is provided in Table 2.2, while representative reactor configurations are illustrated in Figure 2.2 and Figure 2.3.

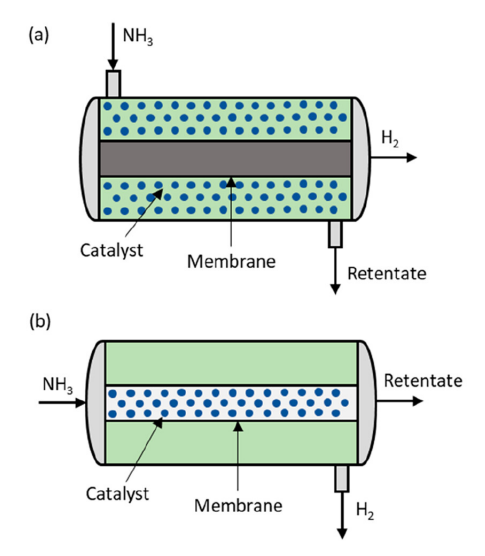


Figure 2.2: Packed-bed membrane reactor: shell (a) and tube (b) configurations.[11].

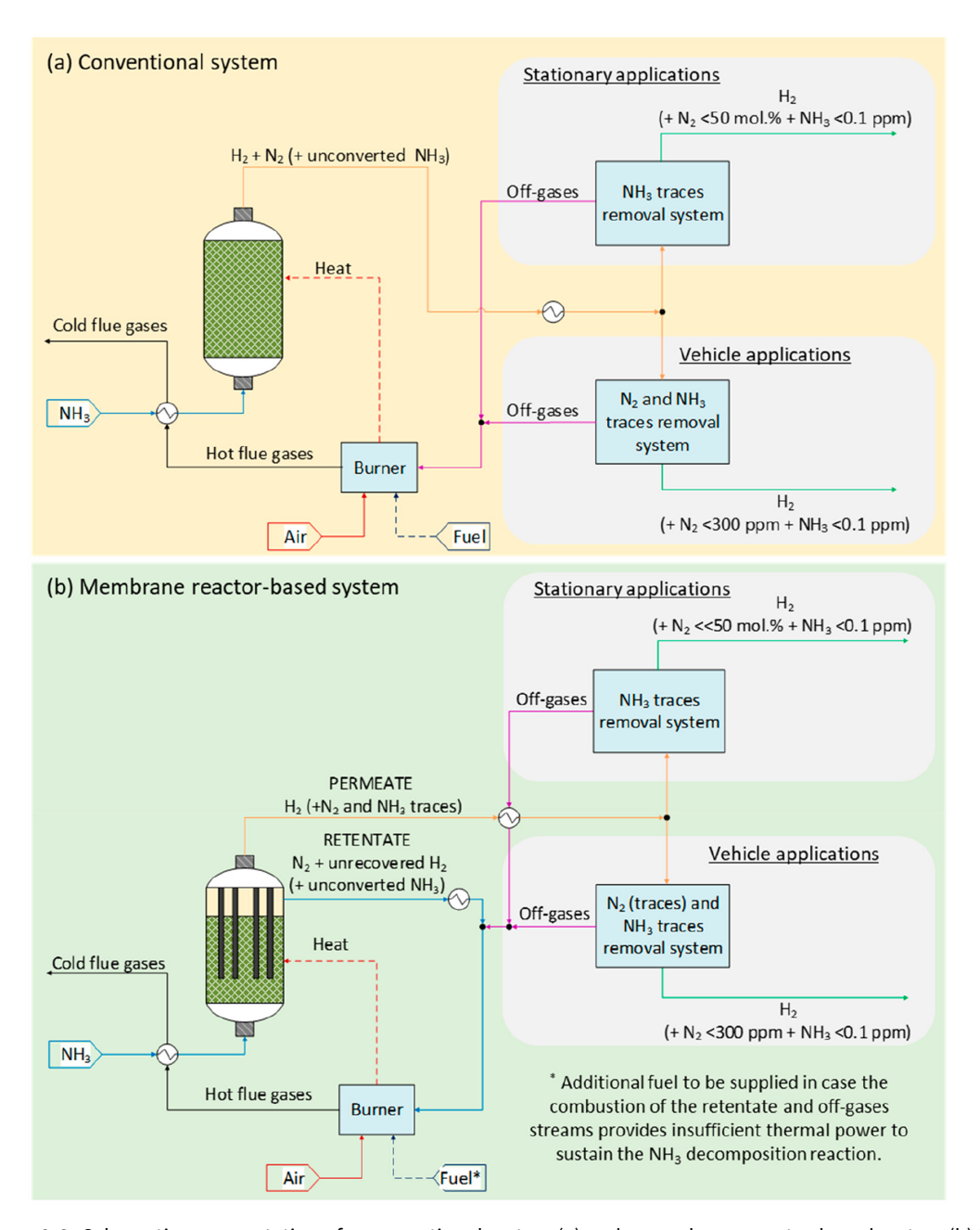


Figure 2.3: Schematic representation of a conventional system (a) and a membrane reactor-based system (b) for hydrogen production via ammonia decomposition [11].

Table 2.2: Illustrative performance envelopes for ammonia decomposition in conventional packed beds (PBR) and catalytic membrane reactors (CMR). Values indicate typical ranges in the literature.

Metric	Conventional PBR	CMR	Notes
Operating temperature	650-700 °C	400-450 °C	CMR lever is low $p_{\rm H_2,perm}$ via sweep or vacuum [12].
NH ₃ conversion	70–99%	>99%	CMR shifts equilibrium and mitigates product inhibition.
H ₂ purity (dry)	~70–80%	>99.7%	Permeate is nearly pure H ₂ for defect-free Pd-alloy films.
Energy efficiency	Baseline	Improved	Lower <i>T</i> and reduced downstream separation duty.
Process integration	Reaction + separate separation	Combined unit	Fewer unit operations; simpler heat integration.

2.2 Hydrogen Permeation in Palladium-Based Membranes

2.2.1 Material Properties and Operating Window

Dense Pd and Pd–alloy membranes are, in their ideal defect-free state, infinitely selective to H_2 . Modern membrane modules employ thin Pd–alloy films (5–20 μ m) deposited on porous supports to provide mechanical strength. Operation is typically conducted between 300–600 °C to ensure high permeability while avoiding the low-temperature $\alpha - \beta$ hydride phase transition, which can cause embrittlement. Alloying palladium with silver (e.g., Pd–Ag 23wt%) is common as it suppresses this critical temperature and improves mechanical robustness and resistance to poisoning [19].

Table 2.3: Qualitative comparison of H₂-separation membrane classes.

Membrane class	Selectivity to H ₂	Typical T	Notes
Dense Pd/Pd-alloy	$ ightarrow \infty$ (defect-free)	300-600 °C	Highest purity; cost/poisoning/embrittlement mitigated by supports and alloying [19].
Microporous ceramic	Moderate (5–100)	300-600 °C	Knudsen/sieving; robust but lower purity.
Polymeric	Low-moderate	≲150 °C	Not suitable for hot NH₃ cracking streams.

2.2.2 The Multi-Step Solution-Diffusion Mechanism

The permeation of hydrogen through a dense palladium-based membrane is a complex, multi-step process involving phenomena at the surfaces, within the bulk metal, and in the surrounding gas phases [13, 15]. The transport of a hydrogen molecule from the high-pressure feed side to the low-pressure permeate side involves a sequence of steps, each presenting a potential resistance to the overall flux. The complete sequence, illustrated in Figure 2.4, is as follows:

1. **External Mass Transfer (Feed Side):** H₂ molecules move from the bulk feed gas to the membrane surface.

- 2. Adsorption and Dissociation: H₂ molecules adsorb and dissociate into H atoms on the surface.
- 3. **Dissolution:** Hydrogen atoms transition from the surface into the bulk palladium alloy.
- 4. **Bulk Diffusion:** Driven by a chemical potential gradient, H atoms diffuse through the metal lattice
- 5. **Transition:** H atoms move from the bulk metal to the permeate-side surface.
- Recombination and Desorption: H atoms recombine to form H₂ and desorb from the surface.
- 7. **Transport in the Porous Support:** H₂ travels through the porous support.
- External Mass Transfer (Permeate Side): H₂ molecules move from the surface into the bulk permeate stream.

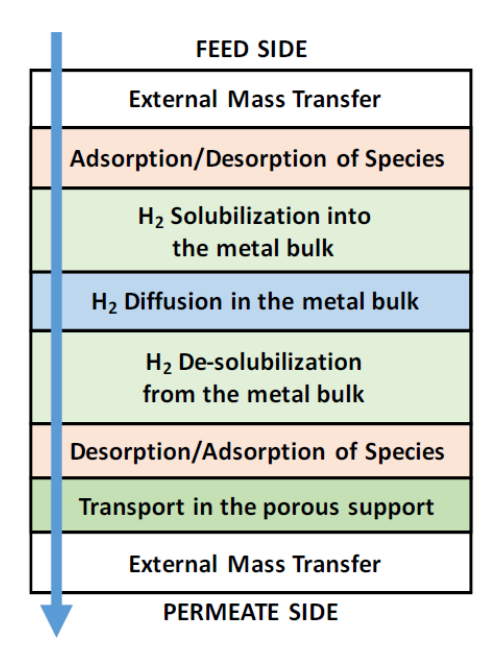


Figure 2.4: The sequence of transport steps for hydrogen permeation through a supported palladium membrane [13].

2.2.3 The Ideal Model: Diffusion-Limited Transport

The foundational framework for quantifying hydrogen permeation is the solution-diffusion model, which is valid under ideal conditions where the diffusion of hydrogen atoms through the bulk palladium lattice (Step 4) is the sole rate-limiting step [13]. This model assumes that all surface reactions are instantaneous (at equilibrium) and that external mass transfer resistances are negligible as depicted in Figure 2.5. It is built upon two principles:

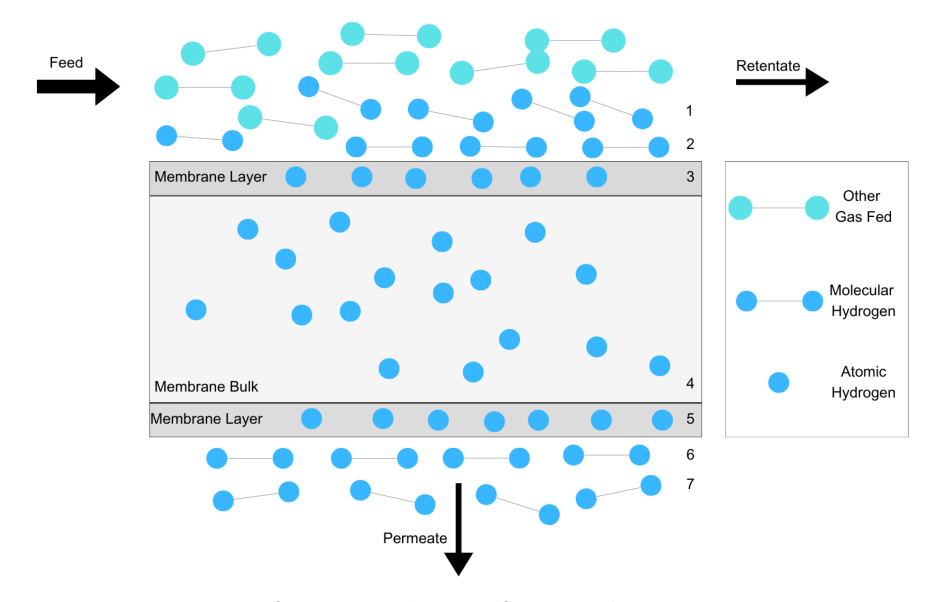


Figure 2.5: Solution-Diffusion mechanism

Fick's First Law states that the steady-state flux (J_H) of atomic hydrogen is proportional to its concentration gradient:

$$J_{\mathsf{H}} = -D\frac{dC}{dx} \tag{2.2}$$

where D is the diffusion coefficient [20].

Sieverts' Law describes the equilibrium solubility, stating that the concentration of dissolved hydrogen atoms (C) in palladium is proportional to the square root of the hydrogen partial pressure ($p_{\rm H2}$) in the adjacent gas phase:

$$C = K_s \sqrt{p_{\text{H2}}} \tag{2.3}$$

where K_S is the temperature-dependent Sieverts' constant.

By integrating Fick's Law across a membrane of thickness L and using Sieverts' Law to define the boundary concentrations, we obtain the classic Richardson-Sieverts' Law for molecular hydrogen flux $(J_{H2} = J_H/2)$:

$$J_{\rm H2} = \frac{DK_{\rm s}}{L} \left(\sqrt{p_{\rm H2, feed}} - \sqrt{p_{\rm H2, perm}} \right) \tag{2.4}$$

The product DK_s is defined as the overall hydrogen permeability of the material, P_H . This gives the most common form of the permeation equation:

$$J_{\rm H2} = \frac{P_H}{L} \left(\sqrt{p_{\rm H2, feed}} - \sqrt{p_{\rm H2, perm}} \right) \tag{2.5}$$

Permeability (P_H) is strongly temperature-dependent, typically following an Arrhenius relationship:

$$P_H = P_0 \exp\left(-\frac{E_p}{RT}\right) \tag{2.6}$$

where P_0 is the pre-exponential factor and E_p is the activation energy for permeation.

2.2.4 Modeling Deviations from Ideality: Analysis of Transport Resistances

In practice, the ideal model's assumptions are often not met, and phenomena other than bulk diffusion can significantly limit the overall flux [13, 21, 22]. A comprehensive model must account for these additional transport resistances.

Gas Phase: External Mass Transfer and Concentration Polarization

The ideal model assumes the hydrogen partial pressure at the membrane surface is identical to that in the bulk gas. However, rapid permeation creates a boundary layer where H_2 is depleted and non-permeating species (e.g., N_2 , NH_3) accumulate. This phenomenon, known as Concentration Polarization (CP), reduces the hydrogen partial pressure at the surface, thereby lowering the true driving force for permeation [23, 24].

CP becomes significant at high flux, low feed velocity, or high concentrations of non-permeating species [25]. Using film theory, the flux across this boundary layer is described by a mass transfer coefficient, k_m :

$$J_{\rm H2} = \frac{k_m}{RT} (p_{\rm H2,bulk} - p_{\rm H2,surface}) \tag{2.7}$$

The coefficient k_m is typically estimated from correlations involving the Sherwood number (Sh), defined as:

$$Sh = \frac{k_m d}{D_{\text{H2,mix}}} \tag{2.8}$$

where d is a characteristic length and $D_{\rm H2,mix}$ is the diffusion coefficient of H_2 in the gas mixture. A challenge remains in applying standard Sh correlations, as many are validated for Schmidt numbers (Sc) > 0.6, whereas Sc for H_2 in heavier gases is typically low (0.2), which can lead to inaccuracies [16].

Membrane Surface: Adsorption, Dissociation, and Inhibition

At lower temperatures (typically < 300 °C), the rates of hydrogen adsorption, dissociation, recombination, and desorption can become slow enough to limit the overall permeation rate [26]. Furthermore, impurities in the feed gas such as NH_3 , N_2 , or CO can competitively adsorb onto the palladium surface, blocking the active sites required for hydrogen dissociation and significantly reducing the flux [27].

This competitive adsorption is often modeled using a multi-component Langmuir isotherm, which describes the fractional surface coverage of a species i (θ_i):

$$\theta_i = \frac{K_i P_i}{1 + \sum_j K_j P_j} \tag{2.9}$$

where K_i is the adsorption equilibrium constant. The ideal permeation model can be modified to account for this inhibition, for example, by relating the reduction in permeance to the surface coverage of the inhibiting species [13].

Membrane Bulk: Non-Ideal Transport in the Metal Lattice

Deviations from ideality also occur within the palladium lattice. At high hydrogen pressures, the assumptions of ideal solubility (Sieverts' Law) and a constant diffusion coefficient begin to fail [28]. A common empirical approach is to modify Sieverts' Law with a pressure exponent, n:

$$J_{\rm H2} = \frac{P_H}{I_{\rm L}} \left(P_{\rm H2, feed}^n - P_{\rm H2, perm}^n \right) \tag{2.10}$$

A value of n = 0.5 indicates bulk diffusion is rate-limiting, while an exponent approaching n = 1 suggests that surface phenomena or external mass transfer are becoming dominant [13]. More mechanistic frameworks, like the Ward and Dao model, explicitly consider the kinetics of each elementary step to predict transitions between different rate-limiting regimes [29].

Porous Support: Multi-Mechanism Transport

The thin palladium film requires a mechanical support to withstand operational pressures. This porous support, while structurally necessary, introduces an additional mass transfer resistance on the permeate side. Gas transport through the support is complex and can occur via three primary mechanisms: molecular diffusion, Knudsen diffusion (dominant when the pore size is smaller than the mean free path of gas molecules), and viscous flow (driven by a total pressure gradient).

The Dusty Gas Model (DGM) is a rigorous framework that combines all three mechanisms to describe multicomponent transport in porous media [15, 30]. The DGM treats the porous solid as a component of giant "dust" particles and considers both molecule-molecule collisions (molecular diffusion) and molecule-wall collisions (Knudsen diffusion). Its general form is a complex, implicit equation relating fluxes to gradients in partial and total pressure. One common formulation is given as [31, 32]:

$$\sum_{i \neq i}^{N_c} \frac{x_i N_j - x_j N_i}{D_{ij,\text{eff}}} - \frac{N_i}{D_{iK,\text{eff}}} = \frac{P}{RT} \frac{dx_i}{dz} + \frac{x_i}{RT} \left(1 + \frac{PB_0}{\mu_{\text{mix}} D_{iK,\text{eff}}} \right) \frac{dP}{dz}$$
(2.11)

where N_i and x_i are the molar flux and mole fraction of component i, P is total pressure, z is the transport coordinate, and $\mu_{\rm mix}$ is the mixture viscosity. The terms on the left represent resistances from molecule-molecule and molecule-wall collisions, while the terms on the right represent the driving forces from mole fraction and total pressure gradients.

The effective transport parameters depend on the intrinsic gas properties and the structure of the porous medium (porosity ϵ , tortuosity τ , and average pore diameter d_p) [30, 24]:

• Effective Knudsen diffusivity ($D_{iK.eff}$):

$$D_{iK,\text{eff}} = \frac{\epsilon}{\tau} D_{iK} = \frac{\epsilon}{\tau} \frac{d_p}{3} \sqrt{\frac{8RT}{\pi M_i}}$$
 (2.12)

where M_i is the molar mass.

• Effective binary molecular diffusivity ($D_{ij,eff}$):

$$D_{ij,\text{eff}} = \frac{\epsilon}{\tau} D_{ij} \tag{2.13}$$

where D_{ij} is the free-space diffusion coefficient.

• Viscous flow permeability parameter (B₀):

$$B_0 = \frac{\epsilon d_p^2}{32\tau} \tag{2.14}$$

Accurately modeling the porous support with the DGM is crucial, especially when a sweep gas is used, as it correctly captures the complex interplay between diffusion and pressure-driven flow. When it is assumed that only pure H_2 travels through the support, the DGM reduces to a one-component form. A truly predictive tool must therefore integrate the resistances from all phenomena described namely, external mass transfer, surface kinetics, bulk transport, and support diffusion, often conceptualized as a resistance-in-series model [13].

2.3 Influence of Operating Parameters and System Design

The performance of a palladium membrane system depends critically on both operating conditions and material properties. Temperature increases permeability via an Arrhenius relationship. The driving force is maximized by minimizing the permeate-side hydrogen partial pressure, either by applying a vacuum or by flowing an inert sweep gas (e.g., nitrogen). The choice involves a trade-off between energy costs and potential mass transfer limitations in the support. Membrane thickness is inversely proportional to flux, favoring thinner films, balanced against mechanical integrity. Finally, alloying palladium with elements like silver improves permeability and resistance to embrittlement and poisoning [33].

2.4 Model Validation and Experimental Correlation

To ascertain the predictive accuracy of the developed reactor model, its outputs are rigorously validated against experimental data [15]. This validation process involves comparing key model predictions, such as ammonia conversion or hydrogen flux, with measurements obtained across a range of operating conditions. A strong correlation between predicted and measured outcomes is essential for establishing the model's reliability for process analysis and design.

The goodness-of-fit is quantified using two primary statistical metrics: the coefficient of determination (R^2) and the Mean Absolute Percentage Error (MAPE). The precise mathematical formulations used for these metrics throughout this work are detailed below.

2.4.1 Coefficient of Determination (R^2)

The coefficient of determination (R^2) measures the proportion of the variance in the dependent variable (experimental data) that is predictable from the independent variable(s) (the model). It provides a

measure of how well the model's predictions replicate the observed outcomes. An \mathbb{R}^2 value of 1 indicates a perfect fit, where the model explains 100% of the data's variability. A value of 0 indicates the model performs no better than a simple mean of the data, while a negative value signifies that the model is an arbitrarily poor fit. It is calculated as:

$$R^{2} = 1 - \frac{\sum_{i=1}^{n_{p}} (y_{i}^{\text{exp}} - \hat{y}_{i})^{2}}{\sum_{i=1}^{n_{p}} (y_{i}^{\text{exp}} - \bar{y}^{\text{exp}})^{2}}$$
(2.15)

where y_i^{exp} are the experimental values, \hat{y}_i are the model's predicted values, \bar{y}^{exp} is the mean of the experimental values, and n_p is the total number of data points. The numerator represents the sum of squared residuals (SSR), and the denominator is the total sum of squares (SST).

2.4.2 Mean Absolute Percentage Error (MAPE)

The Mean Absolute Percentage Error (MAPE) measures prediction accuracy as the average of the absolute percentage errors between predicted and actual values. It is a highly intuitive metric because it expresses the average error in percentage terms, making it easy to interpret. The MAPE is defined as:

MAPE =
$$\frac{100\%}{n_p} \sum_{i=1}^{n_p} \left| \frac{y_i^{\text{exp}} - \hat{y}_i}{y_i^{\text{exp}}} \right|$$
 (2.16)

It should be noted that this definition is undefined when an experimental value $y_i^{\rm exp}$ is zero. In the computational implementation for this work, a small tolerance is introduced in the denominator to ensure numerical stability and prevent division-by-zero errors in such cases.

Chapter 3

Modelling Framework

This chapter presents a comprehensive framework for modeling hydrogen transport through a Pd–Ag supported membrane in a catalytic membrane reactor for ammonia decomposition, operating under crossflow annular hydrodynamics. The model captures the sequential transport processes across three layers: (i) external gas-film mass transfer from the bulk shell-side gas to the membrane surface, (ii) dense-metal permeation through the palladium–silver alloy layer, and (iii) porous transport across the alumina support. Additionally, competitive site-blocking (inhibition) by $\rm NH_3$ on the Pd surface is incorporated into the permeation step using a Langmuir-like multiplicative term. The framework couples axial bulk flow with radial transport across the membrane, ensuring consistent evaluation of local driving forces and interfacial hydrogen partial pressures.

3.1 Scope and Assumptions

The modeling is based on the following key assumptions:

- 1. Isothermal operation at a specified axial temperature
- 2. Uniform total pressure on the shell side for each axial slice, and a permeate side at near ambient pressure with hydrogen purity (ppm-level N_2 in H_2/N_2 experiments)
- 3. The gas properties such as diffusivity and viscosity depend on temperature and mixture composition

The bulk shell-side gas phase is modeled as one-dimensional plug flow, discretized axially, while the membrane is resolved radially at each axial position to capture pressure profiles across its layers. This coupled axial-radial approach ensures accurate representation of both bulk flow evolution and local transport resistances across the composite membrane structure.

Hydrogen transport is governed by the local driving force across each layer, determined by the hydrogen partial pressures at the corresponding interfaces (see Figure 3.1). These interfacial pressures are obtained by solving transport models specific to each layer's governing mechanisms, as detailed in the following sections.

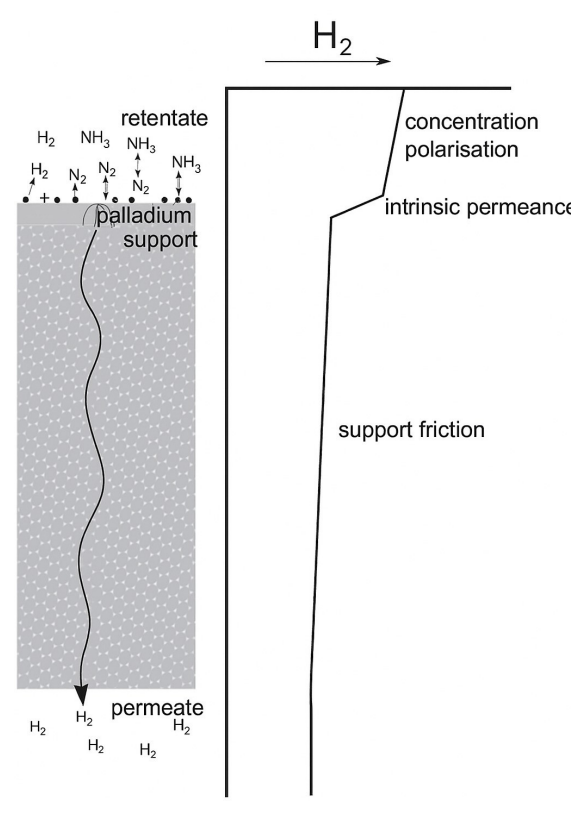


Figure 3.1: Schematic of the transport layers: external gas film, Pd–Ag layer, and porous alumina support. Adapted from Boon et al. (2015) [17].

3.2 Geometry and Operating Envelope

Model validation follows the experimental study of Cechetto *et al.* [12]. Their system employed a tubular Pd–Ag membrane supported by a porous α -Al $_2$ O $_3$ substrate, mounted concentrically within a cylindrical reactor shell. The model focuses on the annular channel between the reactor inner diameter $D_{\rm reactor}$ and the membrane outer diameter $D_{\rm mem}$.

Key geometric and structural parameters are:

- **Membrane**: OD = 14 mm, ID = 10 mm (ID relevant only for the support geometry), length $L \approx 0.190 \, \mathrm{m}$
- Pd-Ag layer: Thickness $t_{\mathrm{Pd}} \approx 4.61 \, \mathrm{\mu m}$
- **Support (top layer)**: Thickness $t_{\rm top} \approx 100 \, \mu {\rm m}$ (dense transition "skin" beneath metal), porosity $\varepsilon \approx 0.35$, tortuosity $\tau \approx 1.25$, pore diameter $d_p \approx 160 \, {\rm nm}$
- **Reactor**: Inner diameter $D_{\rm reactor} \approx 45$ mm, membrane OD $D_{\rm mem} = 14$ mm, giving a hydraulic diameter $D_h = D_{\rm reactor} D_{\rm mem}$

The feed consisted of binary H_2/N_2 mixtures operated at 400–450°C and 1–2 bar(g), while the permeate side was maintained near atmospheric pressure (\sim 1 bar). Under these conditions, hydrogen

purities exceeded 99.99% (with N_2 at only tens of ppm), so that $P_{\rm perm}\approx 1$ bar and $x_{H_2,{\rm perm}}\to 1$. To probe inhibition effects, Cechetto *et al.* repeated the permeation tests using NH₃/H₂ mixtures. Both series of experiments were carried out under the same conditions (400–450°C, 1–2 bar(g)) with inlet hydrogen mole fractions of 0.85, 0.90, and 0.95.

3.3 Governing Equations

Following the theoretical discussion in Chapter 2, the modeling equations are summarized in Table 3.1.

Mechanism	Equation	Remark
External Gas Mass Transfer		
Hydrogen flux	$J_{H_2}(r_{memb}) = k_g c_{tot} \ln \left(\frac{1 - x_{H_2,memb}}{1 - x_{H_2,bullk}} \right)$	Transport through gas boundary layer
Mass transfer coefficient Sherwood number (lam- inar)	$k_g = rac{{ m Sh}D_{H_2,mix}}{d_h} \ { m Sh} = 1.86{ m Gz}^{1/3}$	Laminar flow
Sherwood number (tur- bulent)	$\mathrm{Sh_{turb}} = 0.023\mathrm{Re^{0.83}Sc^{1/3}}$	Turbulent flow
Permeation through Dense Pd-Ag		
Hydrogen flux Permeance	$J_{Pd} = Pe_0(T) \left(p_{H_2, feed}^n - p_{H_2, int}^n \right)$ $Pe_0(T) = Pe_0 \exp\left(-\frac{E_A}{pT} \right)$	$n \approx 0.5 - 0.75$ Pe_0, E_A, n fitted
Porous Support Transport	ov y o i (ki y	U 11
Hydrogen flux	$J_{H_2}^{ ext{porous}} = -rac{D_{H_2}^{ ext{eff}}}{RT} rac{\partial p_{H_2}}{\partial r} - rac{B_0}{\mu_{ ext{mix}}RT} x_{H_2} rac{\partial p_{ ext{tot}}}{\partial r}$ $B_0 pprox rac{d_p^2 arepsilon}{32 au}$	Dusty Gas Model
Knudsen diffusion Effective diffusivity	$\begin{array}{l} B_0 \approx \frac{32\tau}{32\tau} \\ D_{K,H_2} = \frac{d_p}{3} \sqrt{\frac{8RT}{\pi M_{H_2}}} \\ \frac{1}{D_{H_2}^{\text{eff}}} = \frac{\varepsilon}{\frac{\varepsilon}{\tau} D_{K,H_2}} + \frac{y_{N_2}}{\frac{\varepsilon}{\tau} D_{H_2N_2}} \end{array}$	For H ₂ /N ₂ mixture
Film-Membrane	··2 (A412 (11212	
Coupling Flux Surface concentration	$J = J_{\text{mem}}(p_{H_2, surf}, p_{H_2, perm}; T)$ $x_{H_2, surf} = 1 - (1 - x_{H_2, bulk}) \exp\left(\frac{J}{k_r C_{\text{bulk}}}\right)$	Drift correction
Axial Material Balance Material balance	$\begin{split} F_{H_2}^{(i+1)} &= F_{H_2}^{(i)} - J^{(i)} A_i, F_{N_2}^{(i+1)} = F_{N_2}^{(i)} \\ y_{H_2}^{(i)} &= \frac{F_{H_2}^{(i)}}{F_{H_2}^{(i)} + F_{N_2}^{(i)}}, \dot{V}^{(i)} = \frac{(F_{H_2}^{(i)} + F_{N_2}^{(i)})RT}{P_{\text{tot}}} \end{split}$	

Hydrogen recovery frac- HRF = $\frac{\dot{n}_{H_2, perm}}{\dot{n}_{H_2, feed} + 1.5 \, \dot{n}_{\text{NH}_3, in}}$

Ammonia Inhibition

Flux

$$\begin{split} J_{\text{Pd}}^{(\text{with NH}_3)} &= f_{\text{inh}} Pe_0(T) \left(p_{H_2, \, surf}^n - p_{H_2, \, int}^n \right) \\ \Theta_{NH_3} &= \frac{K_{NH_3}(T) p_{NH_3}^m}{1 + K_{NH_3}(T) p_{NH_3}^m}, \quad f_{\text{inh}} = 1 - \Theta_{NH_3} \end{split}$$
Site blocking Langmuir-Hinshelwood

 $K_{NH_3}(T) = K_0 \exp\left(\frac{\Delta H_{\text{ads}}}{RT}\right)$ Inhibition constant

Table 3.1: Governing equations for hydrogen transport and ammonia inhibition.

External Gas-Film Mass Transfer

Hydrogen transport across the gas boundary layer at the cylindrical membrane surface (radius r_{memb}) is governed by the flux equation [16]:

$$J_{H_2}(r_{\text{memb}}) = \frac{D_{H_2 - N_2}}{r_{\text{memb}} \ln\left(1 + \frac{\delta}{r_{\text{memb}}}\right)} c_{\text{tot}} \ln\left(\frac{1 - x_{H_2, \text{memb}}}{1 - x_{H_2, \text{bulk}}}\right) = k_g c_{\text{tot}} \ln\left(\frac{1 - x_{H_2, \text{memb}}}{1 - x_{H_2, \text{bulk}}}\right), \quad (3.1)$$

where k_g is the overall mass transfer coefficient, δ is the boundary layer thickness, and c_{tot} is the total molar concentration. Although the stagnant film model lacks full rigor, it effectively characterizes concentration polarization in Pd-based membranes [34]. The mass transfer coefficient k_g varies with membrane geometry and hydrodynamics, and is related to the Sherwood number (Sh) via:

$$Sh = \frac{k_g d_h}{D_{H_0, mix}},\tag{3.2}$$

$$k_g = \frac{D_{H_2, mix}}{d_h} \cdot Sh,\tag{3.3}$$

where d_h is the hydraulic diameter.

The stagnant film model is commonly interpreted and mathematically validated by Zydney, who proposes that k_g can be treated as a convective coefficient based on a pseudo-concentration [35]. This approach, also utilized by Rohlfs et al., facilitates the determination of k_g using the Sherwood number, defined as the ratio of convective to diffusive mass transport rates [36].

The Sherwood number is determined using empirical correlations that vary with flow conditions. In this study, following the recommendations of Ververs et al. [16], who focused exclusively on Sherwood correlations for calculating the mass transfer coefficient in a system featuring a Pd-based membrane within an empty vessel, the following correlations are applied:

For laminar developing flow, Graetz-type relations are utilized:

$$Sh_{Graetz} = 1.86 \,Gz^{1/3},$$
 (3.4)

$$Sh_{1.615} = 1.615 \,Gz^{1/3},$$
 (3.5)

$$Sh_{Shah-London} = 3.66 + \frac{0.0668 \,Gz}{1 + 0.04 \,Gz^{2/3}},$$
(3.6)

The baseline $Sh = 1.86 \, Gz^{1/3}$ is adopted following sensitivity analyses.

For turbulent flow, a Gnielinski-type correlation is used:

$$Sh_{turb} = 0.023 \,\text{Re}^{0.83} \text{Sc}^{1/3}$$
. (3.7)

The annular gap between the reactor tube (inner diameter $D_{\rm R}$) and membrane (outer diameter $D_{\rm M}$) defines the shell-side flow area $A_{\rm flow}=\frac{\pi}{4}(D_{\rm R}^2-D_{\rm M}^2)$ and hydraulic diameter $d_h=D_{\rm R}-D_{\rm M}$. Local dimensionless numbers are calculated as:

$$Re = \frac{\rho u d_h}{\mu}, \quad Sc = \frac{\mu}{\rho D_{H_2, mix}}, \tag{3.8}$$

with the Graetz number given by $Gz = \operatorname{Re} \operatorname{Sc} \frac{d_h}{L}$.

3.3.2 Permeation Through Dense Pd-Ag

Hydrogen permeation through the Pd-Ag layer is modeled using the modified Sieverts' law:

$$J_{\rm Pd} = Pe_0(T) \left(p_{H_2, feed}^n - p_{H_2, int}^n \right), \tag{3.9}$$

$$Pe_0(T) = Pe_0 \exp\left(-\frac{E_A}{RT}\right),\tag{3.10}$$

where $Pe_0(T)$ is the temperature-dependent permeance with Arrhenius behaviour, and n is the pressure-dependent exponent, usually between 0.5 and 1, as reported in the literature. The parameters Pe_0 , E_A , and n are fitted to experimental data.

3.3.3 Porous Support Transport

Based on the assumption that the palladium layer is perfectly selective towards hydrogen, the transport through the thin alumina support layer is modeled using the one-component dusty-gas model, combining Knudsen diffusion, binary diffusion, and a viscous (Darcy) term for total pressure gradients:

$$J_{H_2}^{\text{porous}} = -\frac{D_{H_2}^{\text{eff}}}{RT} \frac{\partial p_{H_2}}{\partial r} - \frac{B_0}{\mu_{\text{mix}}RT} x_{H_2} \frac{\partial p_{\text{tot}}}{\partial r}, \quad B_0 \approx \frac{d_p^2 \, \varepsilon}{32 \, \tau}, \tag{3.11}$$

$$\frac{1}{D_{H_2}^{\text{eff}}} = \frac{1}{\varepsilon/\tau \, D_{K,H_2}} + \frac{y_{N_2}}{\varepsilon/\tau \, D_{H_2N_2}},\tag{3.12}$$

$$D_{K,H_2} = \frac{d_p}{3} \sqrt{\frac{8RT}{\pi M_{H_2}}},\tag{3.13}$$

where d_p is the characteristic pore diameter, ε is porosity, τ is tortuosity, and B_0 is the hydraulic permeability. Equation (3.11) is solved across the support thickness δ_s , with continuity enforced at the Pd/support interface ($p_{H_2,int}$).

3.3.4 Film-Membrane Coupling and Concentration Polarization

At each axial position, the bulk H_2 mole fraction y_{H_2} is depleted by the permeating flux. A stagnant-film model with finite k_g provides the surface composition:

$$J = J_{\text{mem}} \left(p_{H_2, \, surf}, \, p_{H_2, \, perm}; T \right), \quad x_{H_2, \, surf} = 1 - (1 - x_{H_2, \, bulk}) \exp \left(\frac{J}{k_g \, C_{\text{bulk}}} \right), \tag{3.14}$$

where $C_{\rm bulk}=p_{\rm tot}/(RT)$. The second term accounts for the drift (high-flux) correction, where through-film advection biases the surface composition toward $\rm H_2$.

3.3.5 Ammonia Inhibition

Competitive site-blocking by NH_3 on the Pd surface is modeled using a Langmuir-like multiplicative factor:

$$\Theta_{NH_3} = \frac{K_{NH_3}(T) p_{NH_3}^m}{1 + K_{NH_3}(T) p_{NH_2}^m}, \quad f_{\text{inh}} = 1 - \Theta_{NH_3}, \tag{3.15}$$

$$J_{\rm Pd}^{(\text{with NH}_3)} = f_{\rm inh} Pe_0(T) \left(p_{H_2, \, surf}^n - p_{H_2, \, int}^n \right), \tag{3.16}$$

where the inhibition constant follows van't Hoff temperature dependence:

$$K_{NH_3}(T) = K_0 \exp\left(\frac{\Delta H_{\text{ads}}}{RT}\right). \tag{3.17}$$

Rationale for Inhibition Model Selection

In modeling the inhibitory effect of ammonia, a simple, single-site Langmuir-Hinshelwood (L-H) site-blocking formalism was chosen. This decision was based on a deliberate balance between physical realism, model parsimony, and the information content of the available experimental data. While more

complex inhibition mechanisms are possible (e.g., multi-site adsorption, dissociative adsorption), the L-H model was deemed the most appropriate for the following reasons:

- As demonstrated in Chapter 4, the simple L-H term was remarkably successful in capturing the experimental trend and eliminating the systematic bias. Adding further complexity would introduce additional fitting parameters without a clear, data-driven justification, risking overfitting.
- The fitted enthalpy of adsorption ($\Delta H_{\rm ads} \approx -40$ kJ/mol) strongly supports a mechanism of weak, molecular chemisorption [37]. This aligns perfectly with the foundational assumption of the L-H model: a reversible equilibrium between gas-phase molecules and a single type of adsorbed surface species. It does not support a more complex dissociative mechanism.
- The experimental data consists of flux measurements across the entire membrane. This type of data is ideal for quantifying the magnitude of inhibition but is not well-suited for distinguishing between more subtle mechanistic details (e.g., identifying specific adsorption sites). Distinguishing such effects would require dedicated surface-sensitive experiments, which were outside the scope of this work.

Therefore, the chosen L-H model represents the most robust description of the inhibition phenomenon given the available data, providing a physically-grounded and predictively powerful framework.

3.4 **Axial Material Balance**

Pd-based membranes selectively remove hydrogen from gas mixtures, decreasing both the hydrogen fraction and total flow rate along the membrane length. Because permeation is driven by the hydrogen partial pressure $(p_{H_2} = p \cdot y_{H_2})$, this depletion reduces flux [16]. To capture variations in composition and velocity, the membrane length L is discretized into N axial slices of area A_i (1D) under the assumption of angular symmetry (Figure 3.2). Radial effects are incorporated via an external mass transfer term. The retentate is represented as annular unit cells, with gas flowing axially (z) and permeation occurring radially (r). Mass balances are then applied for hydrogen and other components in each cell [16].

For each slice *i*, the balances are:

$$F_{H_{a}}^{(i+1)} = F_{H_{a}}^{(i)} - J^{(i)}A_{i}, F_{N_{a}}^{(i+1)} = F_{N_{a}}^{(i)}, (3.18)$$

$$F_{H_2}^{(i+1)} = F_{H_2}^{(i)} - J^{(i)} A_i, F_{N_2}^{(i+1)} = F_{N_2}^{(i)}, (3.18)$$

$$y_{H_2}^{(i)} = \frac{F_{H_2}^{(i)}}{F_{H_2}^{(i)} + F_{N_2}^{(i)}}, \dot{V}^{(i)} = \frac{\left(F_{H_2}^{(i)} + F_{N_2}^{(i)}\right) RT}{p_{\text{tot}}}, (3.19)$$

Here, $F_{H_2}^{(i)}$ and $F_{N_2}^{(i)}$ are the molar flows of hydrogen and nitrogen, respectively, while $J^{(i)}$ is the hydrogen molar flux obtained from the permeation model. At each segment, the local mass transfer coefficient, k_g , concentration polarization, and intrinsic flux are computed. The framework predicts both the standard volumetric permeate flow Q_{pred} and the hydrogen recovery fraction (HRF):

HRF =
$$\frac{\dot{n}_{H_2, perm}}{\dot{n}_{H_2, feed} + 1.5 \, \dot{n}_{\text{NH}_2, in}},$$
 (3.20)

which simplifies to $\dot{n}_{H_2,~perm}/\dot{n}_{H_2,~feed}$ for binary $\rm H_2/N_2$ systems.

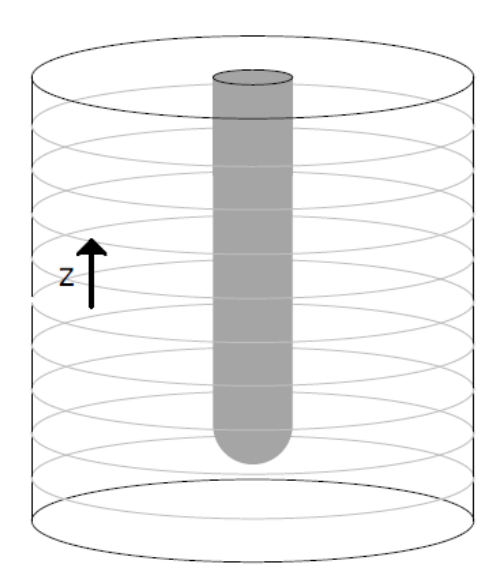


Figure 3.2: Axial discretization of the membrane, modeled as annular unit cells with axial flow and radial permeation, as adapted from [16].

3.5 Numerical Solution

For each axial slice, Equation 3.14 is iterated to ensure consistency between the surface composition and the intrinsic membrane/support solution (Equation 3.16 and Equation 3.11). The Pd/support interface pressure $p_{H_2,\,int}$ is determined by solving the flux mismatch $J_{\rm Pd}(p_{H_2,\,int})-J_{\rm porous}(p_{H_2,\,int})=0$ using a robust bracketed root-finder (Brent's method) or bounded scalar minimization if bracketing fails. Convergence is achieved when $|\Delta J|<1\times10^{-7}\,{\rm mol/(m^2\,s)}$. This process is illustrated schematically in Figure 3.3.

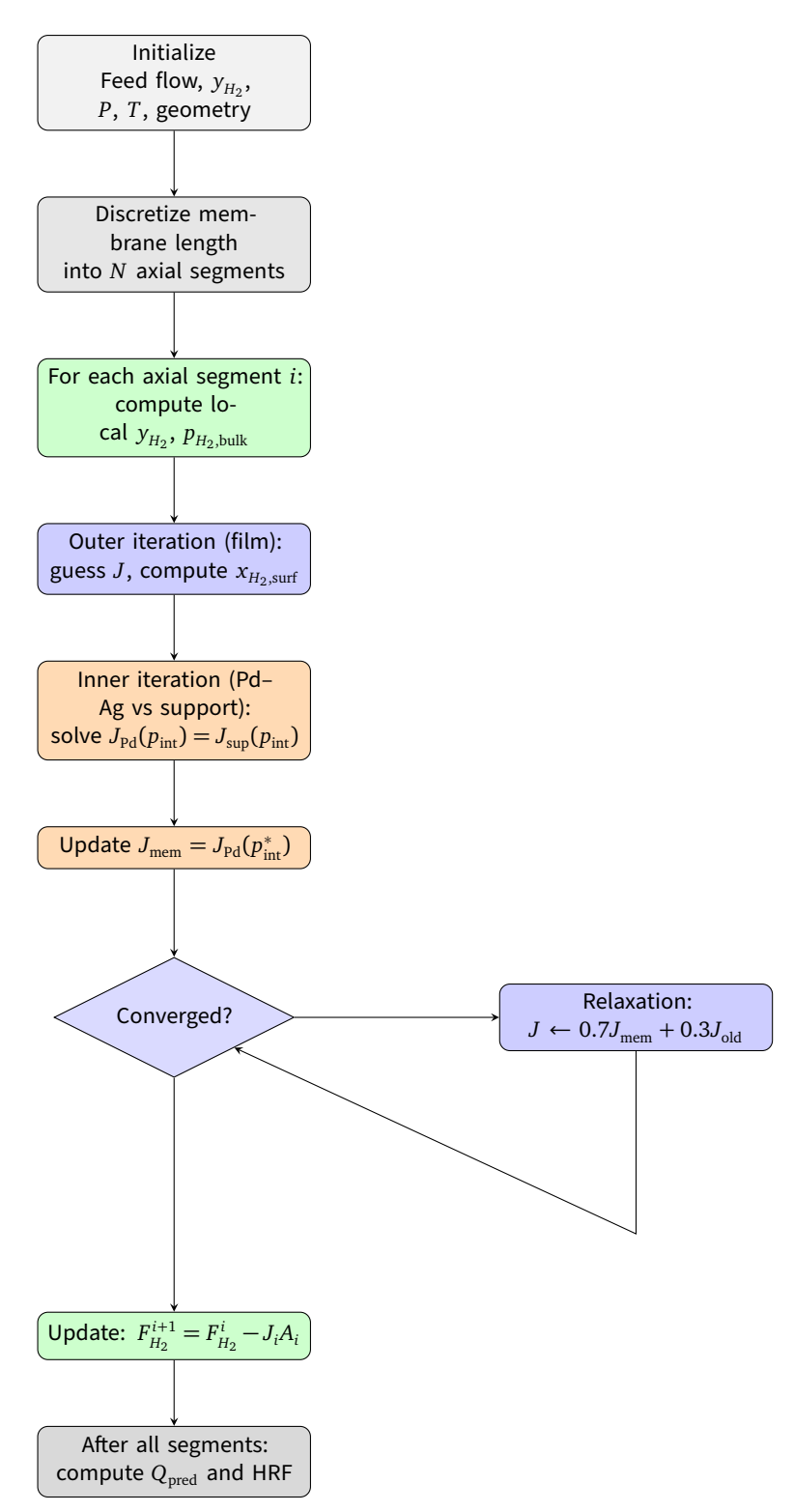


Figure 3.3: Flowchart of the nested iteration strategy for hydrogen flux calculation through Pd-Ag membranes.

3.6 Membrane Reactor Model

A validated, detailed hydrogen permeation model has been developed and is now integrated with a reactor model previously created by Bala, a graduate student in the SPE group. The reactor model compares the performance of a packed bed reactor with that of a packed bed membrane reactor. The membrane reactor model initially employed Richardson's equation, which simplifies all transport processes in the composite membrane into a single equation. The objective of integrating the validated permeation model into the membrane reactor model is to compare the performance of the detailed permeation model with the simplified one. Although the reactor geometry and membrane used in Bala's model differ from those validated in this work, the validated permeation model remains applicable for studying the membrane reactor model. A comparison of the key features between the reactor model and the validated permeation model is presented in Table 3.2.

Feature	Reactor Model	Validated Permeation Model
Primary Goal	Simulate ammonia decomposition in a packed bed membrane reactor (PBMR).	Model and validate the physics of ${\cal H}_2$ permeation through a specific membrane.
Permeation Model	Simplified Sieverts' Law. Uses a basic $J \propto (P_{\rm H_2,ret}^{0.72} - P_{\rm H_2,perm}^{0.72})$ form with a simple Arrhenius term for permeance.	Comprehensive Resistance-in- Series Model. Includes generalized Sieverts' Law for the Pd layer.
Support Resistance	Ignored. Assumes the porous support offers no resistance to flow.	Explicitly Modeled. Uses a corrected Dusty Gas Model (DGM) that accounts for Knudsen and viscous flow of pure H_2 in the support.
Concentration Polarization (CP)	Ignored. Assumes ${\cal H}_2$ concentration at the membrane surface is the same as in the bulk gas.	Explicitly Modeled. Calculates the external mass transfer resistance in the gas film, which is crucial at high fluxes.
NH_3 Inhibition	Ignored. Assumes ammonia has no effect on ${\cal H}_2$ permeation.	Explicitly Modeled. Contains a validated Langmuir-Hinshelwood model for the inhibitory effect of NH_3 .
Reaction Kinetics	Included. Contains a detailed kinetic model for ammonia decomposition.	Not Applicable. Focuses only on the separation process.
Heat Transfer	Included. Contains an energy balance to model temperature changes along the reactor.	Isothermal. Assumes constant temperature.

Table 3.2: Comparison of Reactor Model and Validated Permeation Model Features

Chapter 4

Results and Discussion

4.1 Parameter Estimation Strategy

To distinguish the effects of ammonia inhibition from the baseline membrane performance, a three-step sequential parameter fitting strategy was employed:

- 1. **Intrinsic Permeance**: The intrinsic permeance pre-exponential factor (Pe_0) , activation energy (E_A) , and pressure exponent (n) are determined by fitting the core permeation model in Equation 3.9 to experimental data from non-inhibiting H_2/N_2 mixtures.
- 2. **External Mass Transfer**: The model is subsequently extended to include external mass transfer resistance by introducing a correction factor, α , which is concurrently determined alongside the intrinsic parameters. This factor scales the theoretical mass transfer coefficient (Equation 3.3) to account for uncertainties in the reactor geometry and the selected Sherwood correlation.
- 3. **Ammonia Inhibition**: With the baseline parameters Pe_0 , E_A , n, α held constant at the values obtained from the H_2/N_2 experiments, the inhibition parameters (the pre-exponential factor (K_0) and the enthalpy of adsorption $(\Delta H_{\rm ads})$) are then fitted using experimental data from H_2/NH_3 mixtures via Equation 3.15–Equation 3.17.

The objective function in each step is the minimization of the mean squared error (MSE) between measured and predicted permeate flow rates. For enhanced interpretability, the coefficient of determination (\mathbb{R}^2) and the mean absolute percentage error (MAPE) are also reported. The robustness of this methodology was confirmed through several supplementary analyses, including assessments of model portability, temperature dependence, and sensitivity to support layer properties.

4.2 Baseline Model Validation: H_2/N_2 Permeation

4.2.1 Dataset and Goodness of Fit

The baseline model parameters were calibrated using an experimental dataset for binary H_2/N_2 mixtures from Cechetto et al. [12]. The experiments were conducted at temperatures of $T \in \{400, 425, 450\}^{\circ}$ C,

feed gauge pressures of $p_{\text{feed}} \in \{1,2\}$ bar(g), and inlet hydrogen mole fractions of $x_{H_2,\text{in}} \in \{0.85,0.90,0.95\}$. Fitting the four baseline parameters $\{Pe_0,E_A,n,\alpha\}$ to the H_2/N_2 data yielded:

$$Pe_0 = (3.8-5.0) \times 10^{-3} \; \mathrm{mol} \, \mathrm{m}^{-2} \, \mathrm{s}^{-1} \, \mathrm{Pa}^{-\mathrm{n}} = (1.75-2.31) \times 10^{-8}, \quad \text{(thickness-based, } \delta = 4.61 \; \mu \mathrm{m})$$
 $E_A \approx 16 \; \mathrm{kJ} \, \mathrm{mol}^{-1}, \; n \approx 0.60, \; \alpha \approx 0.68-0.79$

The model achieves excellent agreement with experimental data, yielding $R^2 \approx 0.96$ –0.97 and MAPE ≈ 3.2 –3.5% (Figure 4.2). The ranges for Pe_0 and α reflect a moderate dependency on the chosen laminar Sherwood number correlation (Table 4.2).

The fitted parameters are physically meaningful and consistent with established values for Pd–Ag membranes [37]. The values of $n \approx 0.60$ and $E_A \approx 16$ kJ/mol align well with literature bands ($n \approx 0.5$ –1.0, $E_A \approx 8$ –25 kJ/mol), supporting the internal consistency of the chosen permeation law [13].

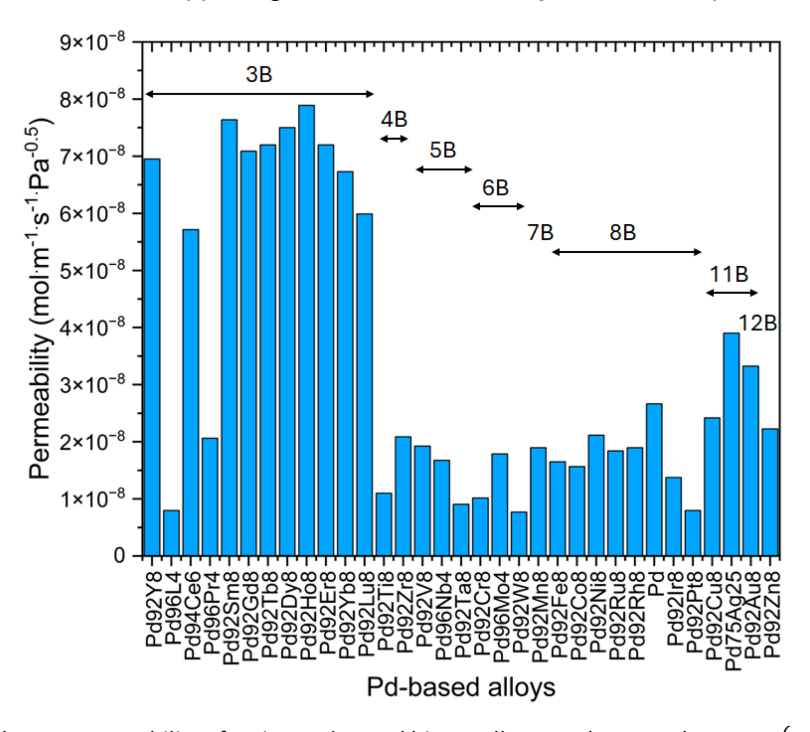


Figure 4.1: Hydrogen permeability of various Pd-metal binary alloy membranes $Pd_x M_{(100-x)}$ (where (100-x) represents the atomic concentration of the solute metal) at 873 K, with the metal M's group in the Periodic Table of Elements indicated. The letter "B" in the figure represents a Group in the Periodic Table of Elements, and the preceding Roman numeral assigned before "B" follows the American Group labelling scheme. Readapted from [37].

4.2.2 Transport Resistance Analysis

To evaluate the interplay between bulk-to-surface transport and membrane permeation, the total driving force for hydrogen permeation, $\Delta P^n = (p^n_{H_2,\text{bulk}} - p^n_{H_2,\text{perm}})$, was partitioned into its constituent resistances. The decomposition (Figure 4.3) shows that transport is governed primarily by the external gas film (approximately 30–50%) and the dense Pd–Ag layer (approximately 50%), with the porous

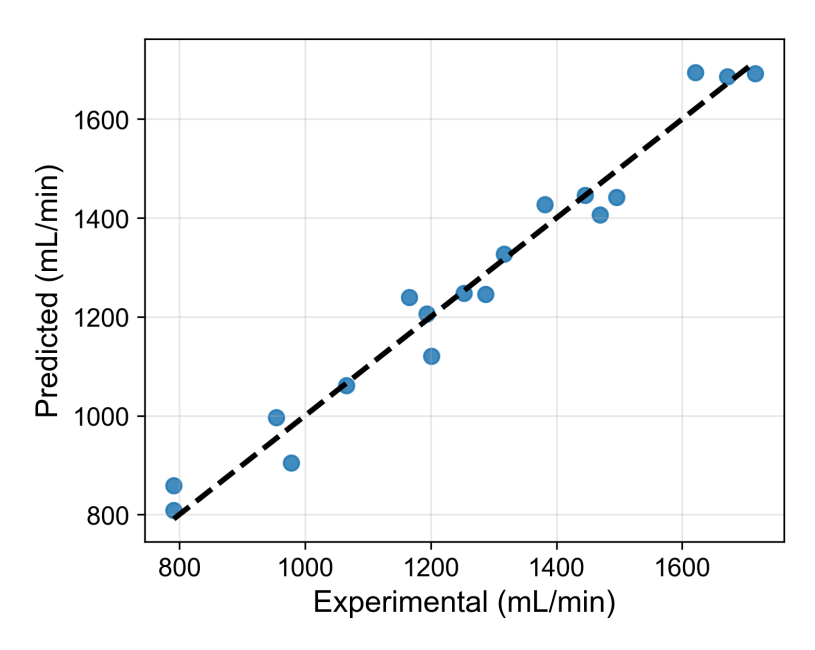


Figure 4.2: Parity plot for the baseline H_2/N_2 permeation model, showing excellent agreement between predicted and experimental flow rates. (R^2 =0.969, MAPE=3.31)

support contributing only a minor fraction (\sim 2%). This confirms that the system operates under a mixed-control regime, where neither diffusion through the film nor permeation through the membrane can be neglected. The negligible role of the support agrees with DGM predictions for the reported morphology ($d_p \approx 100$ –200 nm, $\varepsilon/\tau \approx 0.3$) under pure gas conditions without sweep gas, but could become significant when sweep gas penetrates the support structure [15].

To further probe the severity of concentration polarization, the capacity ratio was defined as

$$\Phi = \frac{k_c C_{\text{bulk}}}{j_{\text{actual}}},\tag{4.1}$$

where k_c is the mass transfer coefficient, $C_{\rm bulk}$ the bulk hydrogen concentration, and $j_{\rm actual}$ the permeation flux. This dimensionless ratio compares the maximum mass transfer supply to the actual permeation demand. As summarized in Table 4.1, the worst-case scenario at $T=450\,^{\circ}{\rm C}$ and P=2 barg yields $\Phi\approx 1.1$ and a Damköhler number $Da_{MT}\approx 1.3$. Both values indicate that external mass transfer and intrinsic permeation resistances are of comparable magnitude. Accordingly, the system resides in a regime where concentration polarization is significant but not solely rate-limiting.

The axial variation of these effects is illustrated in Figure 4.4, which shows that polarization intensifies along the length of the module as the local hydrogen recovery increases. Complementary pressure-ladder plots (Figure 4.5) demonstrate the growing deviation between bulk and surface H_2 partial pressures, highlighting the progressive buildup of film resistance.

Overall, this integrated resistance analysis demonstrates that realistic process models must simultaneously capture both external and intrinsic transport resistances. Neglecting either term, for instance, assuming idealized film-free transport or purely permeation-limited operation, would underestimate system-level hydrogen fluxes and mispredict the required membrane area.

Table 4.1: Detailed mass transfer analysis and sensitivity to support morphology.

Worst-Case Scenario ($T=450^{\circ}$ C, $P=2$ barg, $x_{H_2,feed}=0.85$, $\dot{V}=2.0$ L/min)			
Potential permeation flux, $j_{potential}$	$2.54 \times 10^{-1} \text{mol} \text{m}^{-2} \text{s}^{-1}$		
Maximum mass transfer flux, $j_{\text{max,mt}}$	$1.96 \times 10^{-1} \text{mol} \text{m}^{-2} \text{s}^{-1}$		
Mass transfer coefficient, k_c	$4.61 \times 10^{-3} \mathrm{ms^{-1}}$		
Actual solved flux (inlet), j_{actual}	$1.78 \times 10^{-1} \text{mol} \text{m}^{-2} \text{s}^{-1}$		
Damköhler number, Da_{MT}	1.292		
Capacity ratio, Φ	1.106		

Conclusion: $Da_{MT}\sim 1$ and $\Phi\gtrsim 1$ confirm mixed control. Both mass transfer and permeation resistances must be included for accurate system-level prediction.

Sensitivity to Support Morphology				
R^2 (mean \pm std)	0.961 ± 0.001			
MAPE (%) (mean \pm std)	3.55 ± 0.02			
Film resistance fraction	0.319 ± 0.004			
Membrane resistance	0.661 ± 0.003			
Support resistance	0.021 ± 0.007			

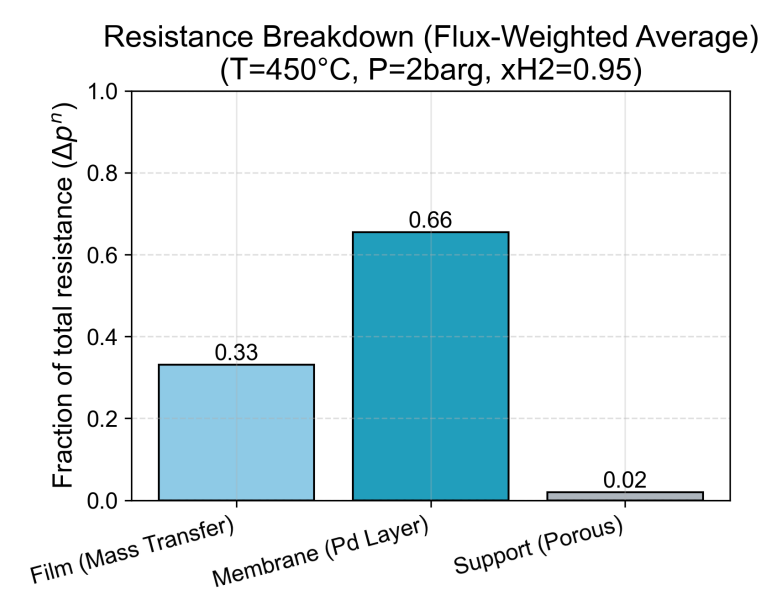


Figure 4.3: Partitioning of transport resistances under representative high-flux conditions. The external gas film and dense Pd–Ag layer dominate, while the porous support is negligible.

4.2.3 Robustness to Sherwood Correlation

To assess the model's sensitivity to the choice of mass transfer correlation, its parameters were refit using three prominent Sherwood number correlations. The results of this analysis are summarized in Table 4.2.

The data highlight the superiority of the Graetz-type correlations, which provide an excellent description of the data with high R^2 values and low MAPE. The fitted scaling factor α for these correlations

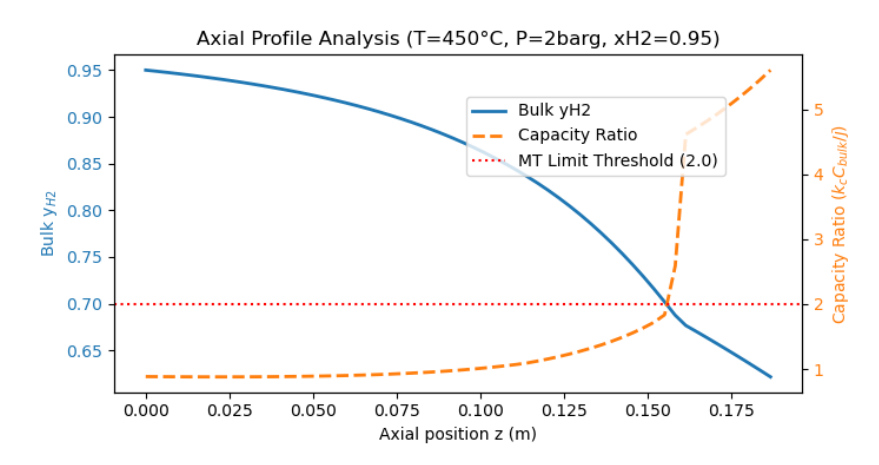


Figure 4.4: Axial evolution of hydrogen recovery and capacity ratio, showing increasing polarization toward the outlet.

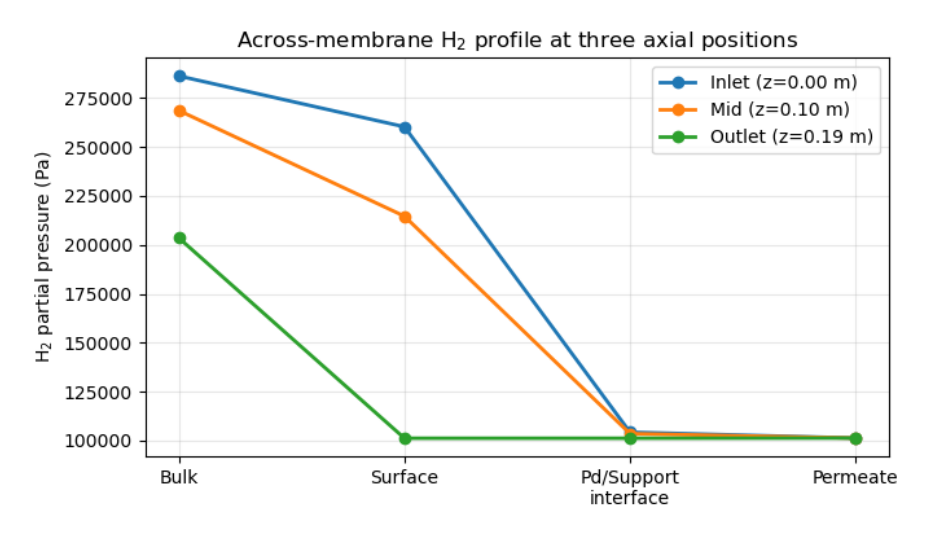


Figure 4.5: Simulated hydrogen partial pressure ladders across the membrane at different axial positions, illustrating the buildup of concentration polarization.

Table 4.2: Summary of fit performance for different Sherwood number correlations. [16, 38]

Correlation	R^2	MAPE (%)	Fitted α
Graetz-186	0.969	3.22	0.68
Graetz-1615	0.962	3.55	0.77
Shah-London	0.941	4.08	0.24

is modest (0.68–0.77), indicating it acts as a mild correction factor rather than compensating for a fundamentally incorrect physical model. Based on these results, the Graetz-186 correlation was selected.

The identification of this correction factor, $\alpha \approx 0.7$, is a significant finding that points to the limitations of applying idealized correlations to real-world systems. This value is not just a simple fitting parameter but likely an empirically derived term that corrects the idealized Sherwood correlation for a combination of complex physical phenomena:

- Entrance Effects and Developing Flow: Standard Sherwood correlations are often derived for fully developed laminar flow. In a reactor of finite length, the hydrodynamic and concentration boundary layers are continuously developing [16]. The fitted $\alpha < 1.0$ can be interpreted as a length-averaged correction that accounts for the fact that the flow never reaches the idealized "fully developed" state.
- Low Schmidt Number (Sc) Behavior: Hydrogen mixtures are characterized by very low Schmidt numbers (Sc $\approx 0.2-0.3$). At low Sc, the concentration boundary layer is much thicker than the momentum boundary layer, and some studies suggest that standard correlations can overpredict the Sherwood number in this regime [39]. The α factor may be empirically correcting for this physical discrepancy.
- Annular Geometry and Curvature Effects: The model uses a hydraulic diameter to apply a correlation likely derived for a simple pipe. In an annular channel, the velocity profile is asymmetric,
 and curvature effects can influence boundary layer development in ways not fully captured by
 the hydraulic diameter concept alone.

In summary, the factor α serves as a robust lumped parameter that corrects for these real-world effects, ensuring the model remains predictive without being overly sensitive to the specific choice of correlation.

4.3 Modeling Ammonia Inhibition Effects

4.3.1 Baseline Model Performance on H_2/NH_3 Mixtures

Application of the baseline model to the H_2/NH_3 dataset, without an inhibition term, resulted in a notable decrease in predictive accuracy ($R^2\approx 0.83$, MAPE $\approx 8.9\%$). More importantly, the model exhibited systematic, composition-dependent prediction errors, indicative of a missing physical phenomenon—namely, competitive adsorption and site-blocking by ammonia. The parity plot further revealed overestimation of H_2 flux at higher NH $_3$ fractions, with numerous points above the 1:1 line (predicted > experimental, (Figure 4.6)). Residuals plotted against $x_{\rm NH}_3$ were positive across all examined NH $_3$ concentrations (\sim 5, 10, 15%) and increased in magnitude with $x_{\rm NH}_3$ (Figure 4.7), confirming that the model systematically overpredicted H_2 flux in the presence of NH $_3$ when Pd parameters were fixed from H_2/N_2 data.

4.3.2 Fitting a Langmuir-Hinshelwood Inhibition Model

To account for inhibition, a site-blocking term based on a Langmuir-Hinshelwood formalism was introduced. Two nested models were considered: a temperature-independent model (Model A, with constant K_0) and a temperature-dependent van't Hoff model (Model B, with K_0 and $\Delta H_{\rm ads}$). Both models substantially improved predictive performance, with Model A yielding $R^2 \approx 0.86$ –0.87 and MAPE ≈ 6.3 –6.4% (Figure 4.8).

Inclusion of the inhibition term effectively removed the systematic bias observed in the baseline model, demonstrating that a composition-dependent site-blocking mechanism is the primary factor

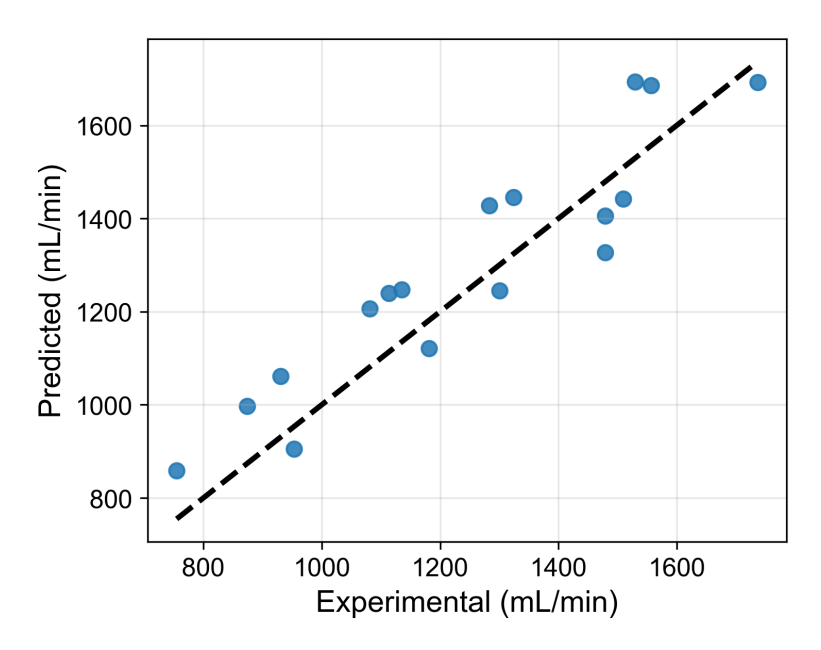


Figure 4.6: Parity plot for H_2/NH_3 mixture - NO inhibition, showing excellent agreement between predicted and experimental flow rates. (R^2 =0.829, MAPE=8.86)

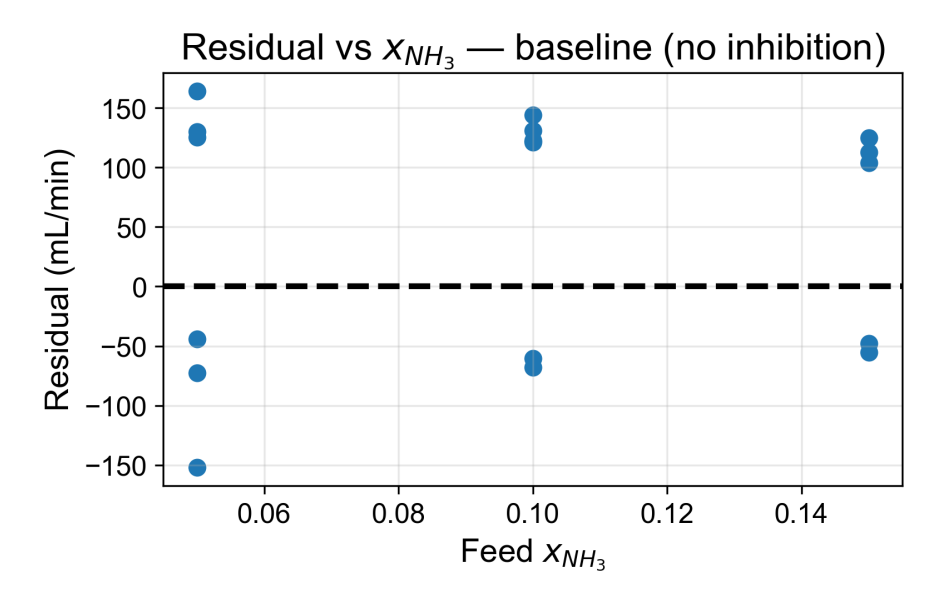


Figure 4.7: Baseline H_2/NH_3 Residuals versus feed x_{NH_3} . Systematic positive bias grows with NH_3 , indicating missing inhibition physics.

governing the reduced $\rm H_2$ flux in the presence of NH $_3$ (Figure 4.9). These results confirm that competitive adsorption of ammonia must be explicitly considered to accurately capture the observed permeation behavior.

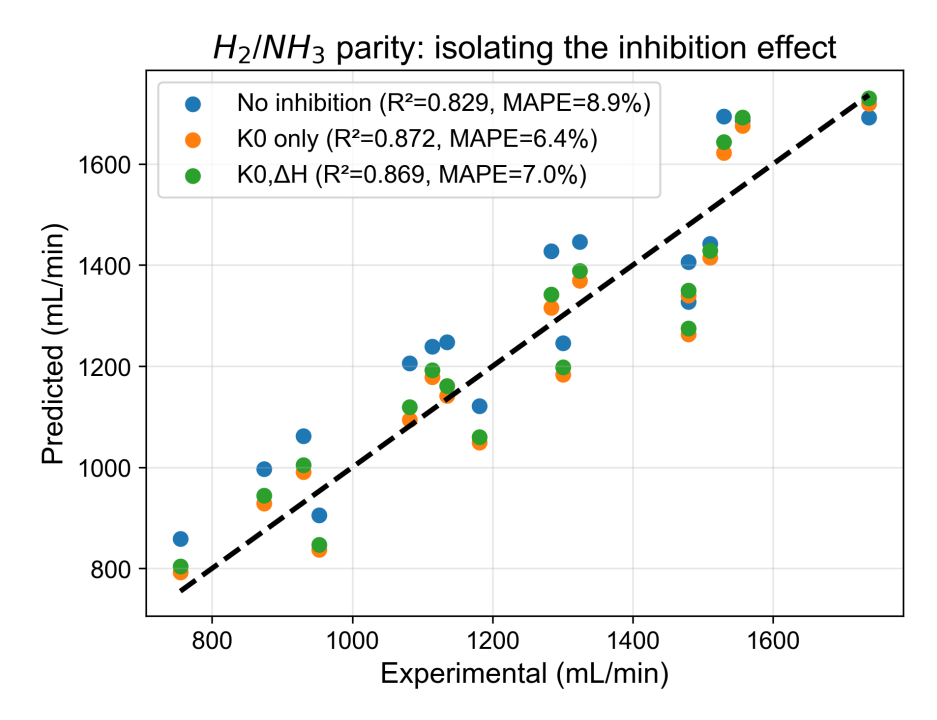


Figure 4.8: Comparison of parity plots for H_2/NH_3 mixtures: the baseline model (blue), the temperature-independent inhibition model (orange), and the full van't Hoff model (green).

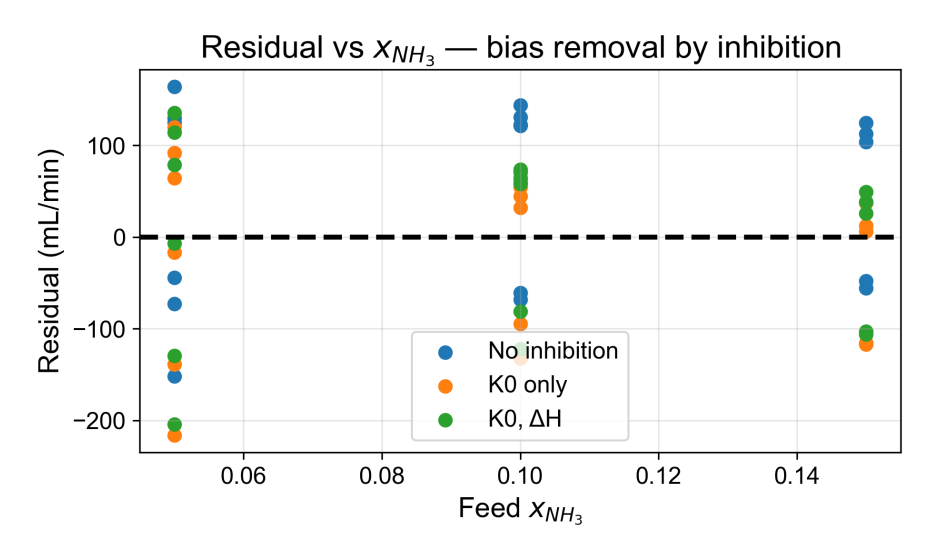


Figure 4.9: Residuals versus feed $x_{\rm NH_3}$ for all three models. Incorporation of the inhibition term (orange and green) removes the systematic bias present in the baseline model (blue).

4.4 Model Selection and Robustness Analysis

4.4.1 Temperature Dependence of Inhibition

The performance of the temperature-independent model (Model A) is nearly identical to that of the full van't Hoff model (Model B). This suggests that over the experimental temperature range of 400–450°C, the temperature dependence of ammonia adsorption is weak. The more parsimonious K_0 -only model is therefore an adequate descriptor of the inhibition effect and is selected as the primary model.

4.4.2 Independent Per-Temperature Fits and Van't Hoff Analysis

To further investigate the temperature dependence, the adsorption constant K was fitted independently at each temperature. A subsequent van't Hoff regression using these values $(\ln K \text{ versus } 1/T)$ gives a modest apparent enthalpy of adsorption, $\Delta H_{\rm ads} \approx -40$ kJ/mol (Figure 4.10). The negative sign and modest magnitude of this enthalpy are consistent with a weak, exothermic adsorption process, such as physisorption or weak chemisorption [40, 41].

Although limited quantitative data exist for ammonia adsorption enthalpies on palladium surfaces, the fitted value obtained here aligns well with expectations and with the few reported values available in the literature, thereby adding credibility to the physical interpretation of the model. Studies on single-crystal palladium surfaces have reported adsorption enthalpies for molecular chemisorption in the range of -50 to -80 kJ/mol [42]. Alloying palladium with silver is known to weaken adsorbate interactions through both electronic and geometric effects, resulting in a less exothermic adsorption enthalpy [43, 40]. Thus, a value of approximately -40 kJ/mol on a Pd-Ag alloy is consistent with these trends and supports the model assumption that inhibition arises from competitive molecular adsorption rather than a more complex surface reaction. Representative reported values for ammonia adsorption enthalpies are summarized in Table 4.3.

This analysis reinforces the conclusion that the temperature dependence of inhibition is too weak within this operational window to justify including $\Delta H_{\rm ads}$ in the primary, more parsimonious model.

Surface	Enthalpy (eV)	Enthalpy (kJ/mol)	Method	Reference
Pd ₃ Ag - fcc	-0.72 to -0.75	-69 to -72	DFT	Peters et al. [27]
Pd(111)	-0.84	-81	At 623 K; DFT.	Småbråten et al. [43]
Pd(111)-Top site	-0.68	-66	DFT.	Stolbov et al. [41]
Pd(111)- FCC hollow	-0.47	-45	DFT.	Stolbov et al. [41]

Table 4.3: Ammonia Adsorption Enthalpies on Pd-Based Surfaces

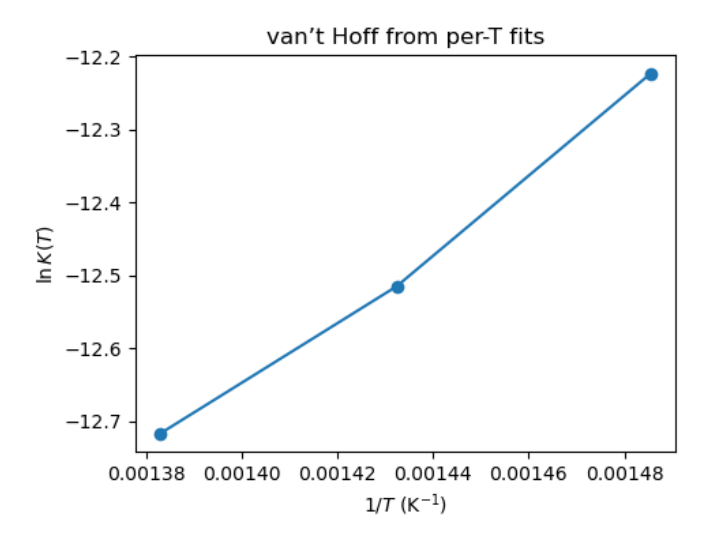


Figure 4.10: Van't Hoff plot derived from fitting the adsorption constant *K* independently at each temperature. The shallow slope indicates a weak temperature dependence.

4.5 Membrane Reactor Model: Comparing Simplified and Mechanistic Permeation Models

This section evaluates the performance of a packed bed membrane reactor (PBMR) by comparing a simplified permeation law against a mechanistic model that integrates Pd–Ag membrane permeance, porous support resistance, and external mass transfer with drift-flux correction. The analysis leverages key performance metrics: H_2 recovery, NH_3 conversion, permeate H_2 purity, and permeate H_2 molar flow as illustrated in Figure 4.11. Additionally, reactor geometry, temperature profiles, concentration distributions, and flux behaviors are examined to provide a comprehensive understanding of the models' predictions, as summarized in Table 4.4 and Table 4.5, and visualized in Figure 4.13 and Figure 4.14.

4.5.1 Reactor Geometry and Operating Conditions

The PBMR's geometric parameters, critical to understanding permeation behavior, are detailed in Table 4.4. The reactor features a 30 mm inner diameter, a 14 mm membrane support, and a thin 7 μ m Pd–Ag layer, with a total membrane surface area of $0.010\,07\,\text{m}^2$. The active membrane zone spans 0.204 m, following a 0.025 m entrance length. Catalyst (10 g) and SiC diluent (170 g) ensure efficient reaction and flow distribution.

4.5.2 H₂ Recovery

As shown in Figure 4.11 (top left), the mechanistic model predicts higher $\rm H_2$ recovery across the temperature range of 350–450°C, outperforming the simplified PBMR law by 6–12 percentage points, with the largest divergence at 375–400°C. This is due to the mechanistic model's detailed flux expression, which accounts for Pd–Ag permeance (with fitted parameters Pe_0 , n, E_a), porous support resistance, and an external film mass-transfer coefficient with drift-flux correction ($\alpha \approx 0.68$). In contrast, the simplified

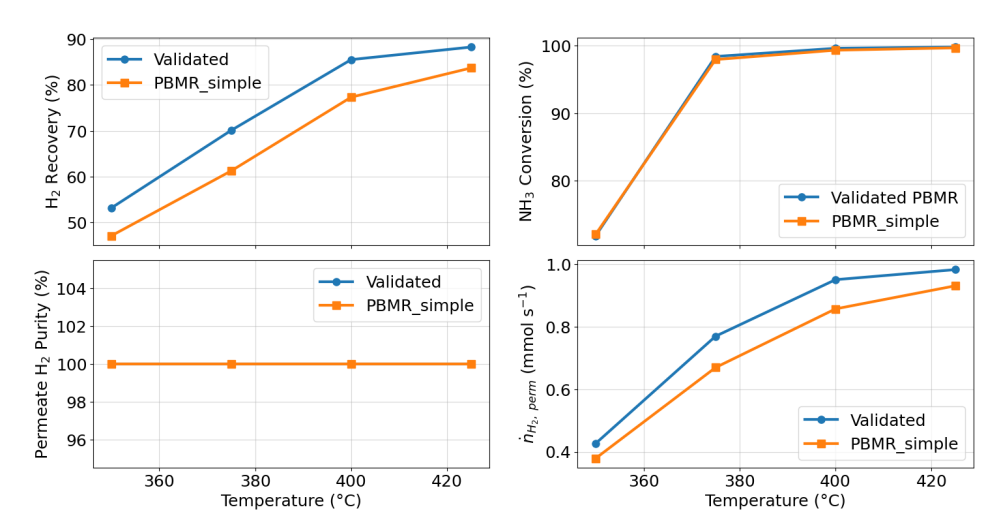


Figure 4.11: Comparative performance plots of the simplified PBMR permeation law (orange) and the validated mechanistic model (blue). Panels show: H_2 recovery (top left), NH_3 conversion (top right), permeate H_2 purity (bottom left), and permeate H_2 molar flow (bottom right).

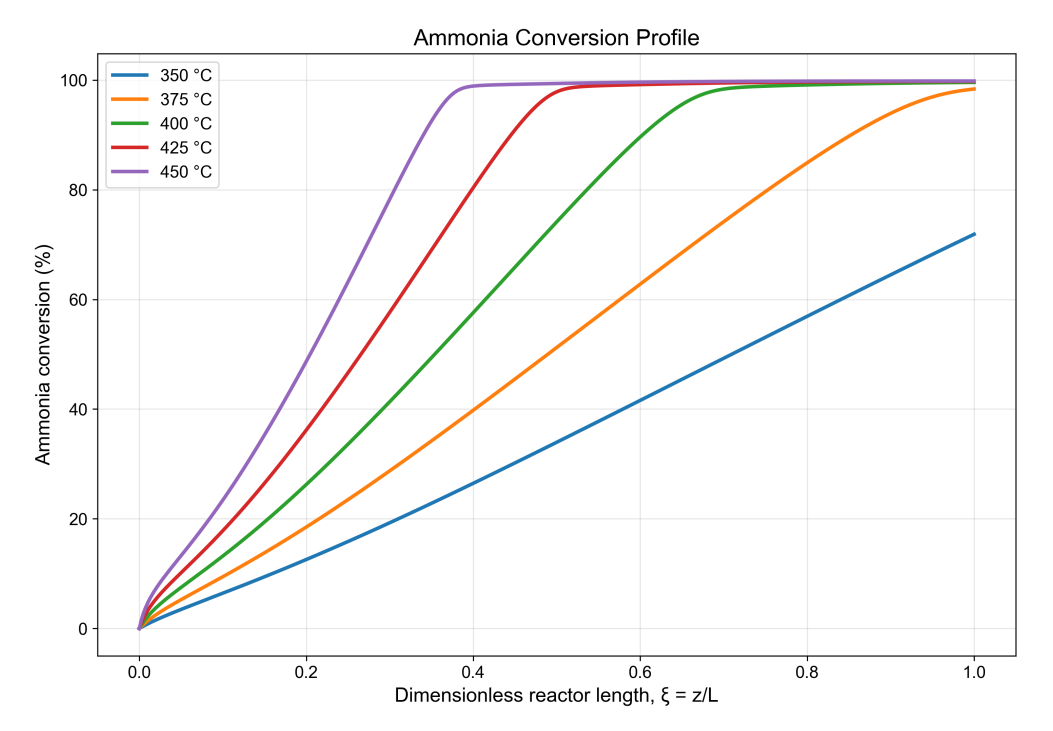


Figure 4.12: Ammonia conversion profile along the reactor

law lumps all the resistance effects together, which, in effect, could be underestimating the effective permeance. Both models show a monotonic increase in recovery with temperature, driven by enhanced surface kinetics and permeance, as illustrated in the temperature profile (Figure 4.13, Top).

Design implication: The simplified law's conservative recovery predictions lead to oversized membrane areas, ensuring a safety margin but potentially increasing costs.

Table 4.4: Geometric Parameters of the Packed Bed Membrane Reactor (PBMR)

Parameter	Description	Value
Reactor Inner Diameter	Inner diameter of the reactor tube	30 mm
Membrane Support Diameter	Outer diameter of the support structure	14 mm
PdAg Layer Thickness	Thickness of the palladium-silver membrane layer	7 μm
YSZ Layer Thickness	Thickness of the yttria-stabilized zirconia layer	1 μm
Membrane Outer Diameter	Total outer diameter of the membrane assembly	14.016 mm
Cross-Sectional Area	Annular area for gas flow	0.000553 m^2
Reactor Length	Total length of the reactor bed	0.229 m
Entrance Length	No-membrane zone at the reactor entrance	0.025 m
Membrane Zone Length	Length of the active membrane zone	0.204 m
Membrane Surface Area	Exposed area for hydrogen permeation	$0.01007 \mathrm{m}^2$
Catalyst Mass	Mass of the catalyst packing	10 g
SiC Diluent Mass	Mass of the silicon carbide diluent	170 g

4.5.3 NH₃ Conversion

 NH_3 conversion, depicted in Figure 4.12, mirrors H_2 recovery trends Figure 4.11 (top right). Above 375°C, both models predict near-complete conversion, with negligible differences due to strong H_2 removal shifting the equilibrium. At 350°C, the mechanistic model yields slightly higher conversion, as its enhanced H_2 permeation further drives the reaction, as seen in the H_2 concentration profile (Figure 4.13, bottom). The mole fraction profiles (Figure 4.14, bottom) highlight how the membrane zone accelerates H_2 production and removal.

Design implication: Conversion differences are minimal at high temperatures or under standard operating conditions. Divergence may occur at lower temperatures or higher space velocities, where H_2 removal significantly impacts equilibrium.

4.5.4 Permeate H₂ Purity

Both models predict near-100% H_2 purity in the permeate stream (Figure 4.11, bottom left), a result of the shared assumption of perfect Pd selectivity and zero NH_3/N_2 crossover. This idealized behavior holds across all temperatures, as no leakage or defects are modeled.

It is important to note that distinguishing the models' purity predictions requires introducing non-ideal effects, such as support leakage or defect-related transport, which are not considered here.

4.5.5 Permeate H₂ Molar Flow

The permeate H_2 molar flow (Figure 4.11, bottom right) follows the recovery trend, with the mechanistic model predicting higher flows across all temperatures, peaking at 375–400°C. The H_2 flux profile (Figure 4.14, top) shows the flux starting at $\xi=0.25$, peaking where the driving force is maximal, and declining as H_2 is removed. The mechanistic model's higher permeance results in greater H_2 extraction for a fixed membrane area.

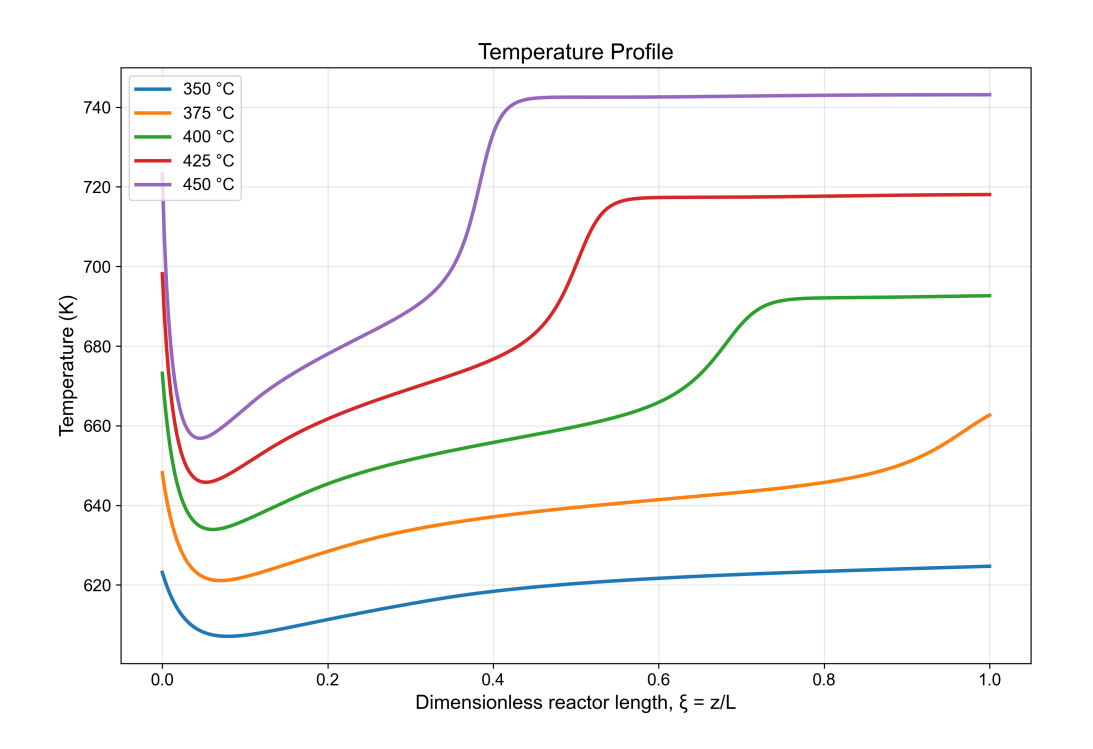
Design implication: The simplified law underestimates H_2 flow, leading to conservative membrane sizing, similar to its impact on recovery.

4.5.6 Summary of Model Comparison

Table 4.5 consolidates the performance differences between the simplified PBMR law and the mechanistic model. The mechanistic model consistently outperforms in H_2 recovery and permeate flow, particularly at 375–400°C, due to its comprehensive flux formulation. Both models align on near-complete NH_3 conversion at high temperatures and idealized H_2 purity. The simplified law serves as a conservative design tool, predicting larger membrane areas than necessary, while the mechanistic model provides more accurate predictions across operating conditions.

Table 4.5: Comparison of simplified PBMR law vs. validated mechanistic permeation model across performance metrics.

Metric	Simplified PBMR Law	Mechanistic Model	Design Implication
H ₂ Recovery vs <i>T</i>	Underpredicts recovery; ~6–12 percentage points lower than mechanistic.	Higher recovery across all <i>T</i> ; largest gap at 375–400°C.	Using simple law over- sizes membrane area (conservative design).
NH_3 Conversion vs T	Similar to mechanistic above ~375°C (near complete). Slightly lower at 350°C.	Nearly complete conversion above 375°C; marginally higher at 350°C due to stronger H ₂ removal.	Conversion differences negligible at high T ; divergence only under harsher conditions (low T , high space velocity).
Permeate H ₂ Purity	~100% (idealized).	~100% (identical).	No distinction unless non- H_2 crossover (NH_3/N_2 leakage, defects) is modeled.
Permeate H_2 Flow $\dot{n}_{H_2, perm}$	Lower across all T ; tracks recovery panel.	Higher across all <i>T</i> ; largest gap at 375–400°C.	For fixed area, mechanistic predicts more H ₂ ; simple law oversizes membrane (conservative).



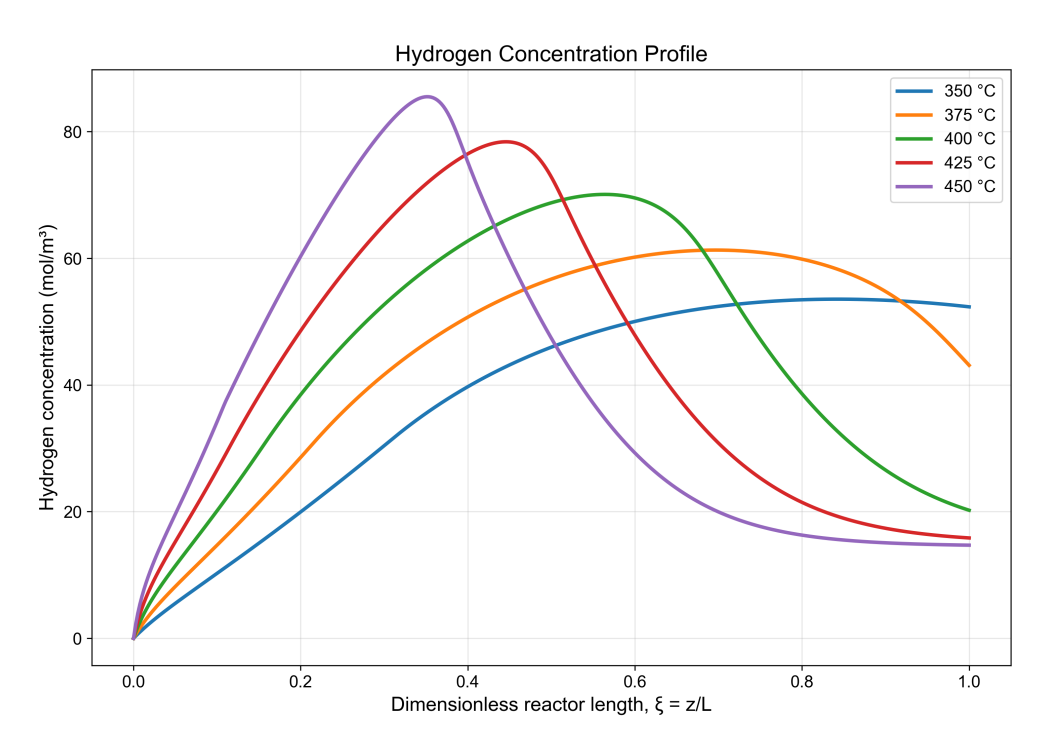
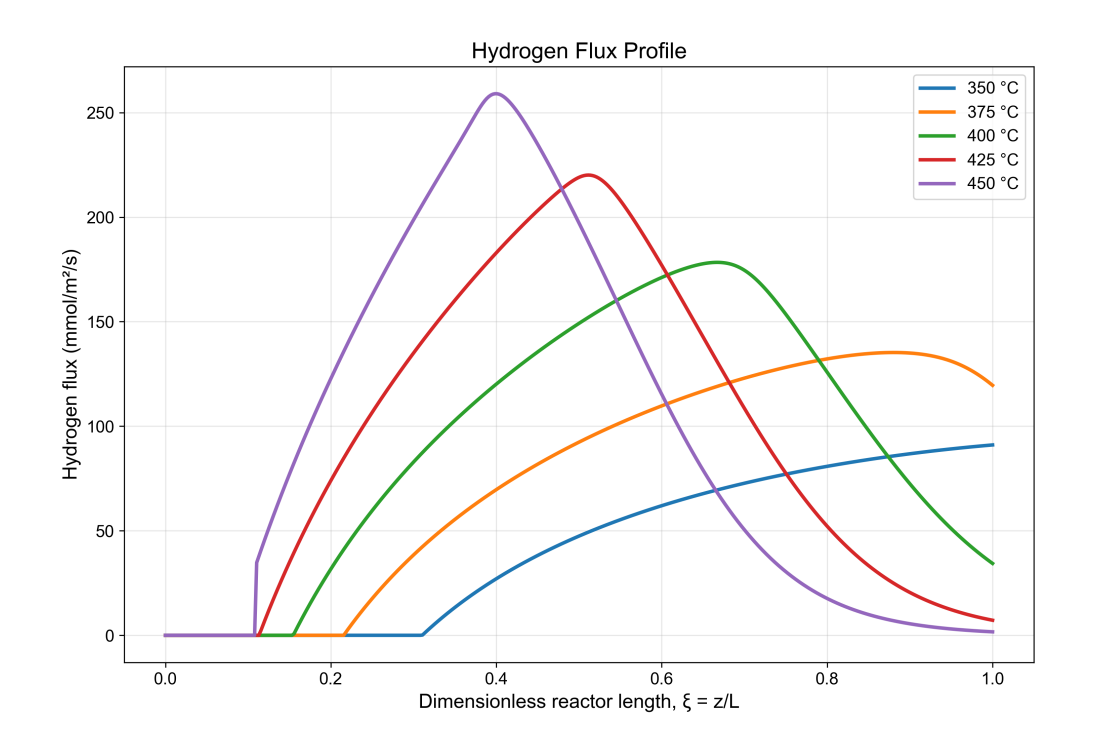


Figure 4.13: (Top)Temperature profile along the reactor, showing inlet temperatures (350–450°C), (Bottom) $\rm H_2$ concentration, peaking due to $\rm NH_3$ decomposition, then declining in the membrane zone.



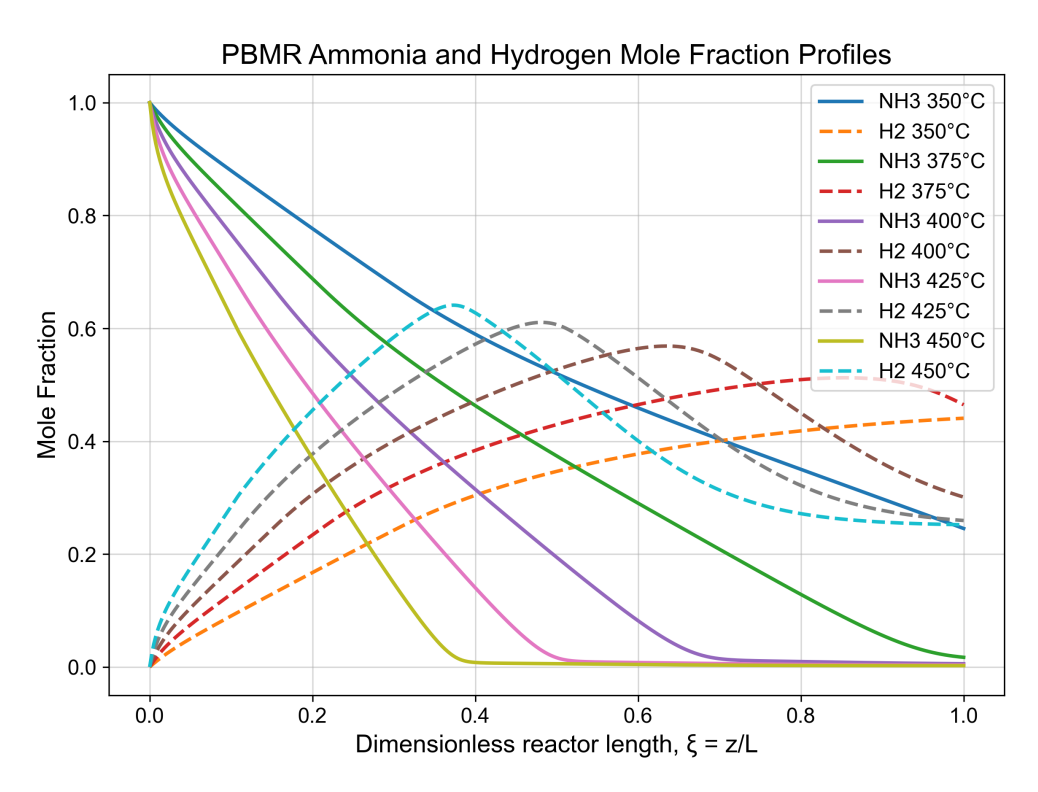


Figure 4.14: (Top) H_2 flux starting at $\xi=0.25$, peaking where driving force is maximal, then declining, (Bottom)N H_3 and H_2 mole fractions; membrane zone accelerates H_2 production and removal.

Chapter 5

Conclusions and Outlook

5.1 Conclusions

This work developed and validated a multi-physics permeation model that quantitatively describes hydrogen transport through a Pd–Ag membrane, both in the absence and presence of ammonia. A robust baseline description was first established for non-inhibiting H_2/N_2 mixtures, coupling external film diffusion, an Arrhenius-type permeance law for the dense Pd–Ag layer, and a Dusty Gas Model for the porous support. The model reproduced experimental data with excellent accuracy ($R^2 \approx 0.97$, MAPE $\approx 3.2–3.5\%$). Transport resistance analysis revealed that flux is co-limited by the palladium layer and external mass transfer, while the porous support plays only a minor role under the investigated conditions.

When extended to H_2/NH_3 mixtures, the baseline model systematically overpredicted flux, indicating the presence of inhibition. Incorporation of a physically grounded Langmuir–Hinshelwood site-blocking term, $1/(1+Kp_{\rm NH_3})$, resolved this discrepancy and captured experimental trends. The fitted parameters identified ammonia as a moderately strong inhibitor, with $K_0 \sim 10^{-6}~{\rm Pa}^{-1}$ and an adsorption enthalpy of $\Delta H_{\rm ads} \approx -40~{\rm kJ\,mol}^{-1}$. The inhibition weakens above $400^{\circ}{\rm C}$, and a simplified temperature-independent form was found sufficient across the studied range. Cross-validation confirmed both predictive robustness and parameter portability.

Beyond regression, a mechanistic model was established that provides a foundation for reactorscale simulations of ammonia decomposition in catalytic membrane reactors. This framework enables detailed assessment of the coupled effects of kinetics, mass transfer, and inhibition.

In summary, this thesis quantitatively isolated the inhibitory effect of ammonia on hydrogen permeation and developed a predictive, physics-based model. The findings strengthen confidence in Pd–Ag membranes for ammonia-related processes such as decomposition for hydrogen production, while underscoring the importance of optimizing external mass transfer to fully exploit membrane performance. performance potential.

5.2 Recommendations

Building upon this foundation, several avenues are recommended for advancing both fundamental understanding and practical application:

5.2.1 Experimental Validation and Parametric Expansion

Conduct permeation experiments at elevated pressures and a wider temperature range (350–550°C).
 Such data would test extrapolation capability and expose conditions where support resistance or stronger inhibition may become significant.

5.2.2 Model Refinement and Extension

- Microkinetic modeling: Replace the phenomenological inhibition term with an elementary-step
 microkinetic framework encompassing H₂ dissociation, NH₃/N₂ competition, surface diffusion,
 and desorption. This would offer mechanistic insight and predictive transferability to other
 catalysts or inhibitors.
- CFD coupling: Eliminate reliance on empirical Sherwood correlation and correction factors by coupling permeation physics into 2D/3D CFD simulations of membrane modules. This would rigorously describe flow, concentration profiles, and transport, yielding a geometry-independent model.

5.2.3 Application and System-Level Integration

- **Membrane reactor simulation:** The integration of the permeation model developed in this work and the reactor model developed by Bala can enable reactor-scale optimization of design and operating conditions.
- **Techno-economic analysis (TEA):** Incorporate the reactor model into process simulators (e.g., Aspen Plus) to assess the real-world impact of ammonia inhibition on efficiency, costs, and hydrogen production economics.

5.3 Future Outlook

The minimal inhibition model, though effective, assumes single-site Langmuir blocking and does not yet resolve elementary adsorption barriers. Moreover, external transport was simplified, though its role was found to be secondary. Addressing these limitations through microkinetic refinement and CFD-based transport models will further enhance predictive accuracy.

Most importantly, the results show that ammonia inhibition is weak and manageable above 400°C. This establishes Pd–Ag membranes as promising candidates for ammonia decomposition membrane reactors, provided that design focuses on: (i) maximizing gas velocities to alleviate polarization, (ii) maintaining high membrane surface area density, and (iii) employing thin, highly permeable supports.

By extending this validated component model to full reactor and process-level simulations, the insights from this thesis can directly inform the design and commercialization of next-generation Pd–Ag membrane reactors, accelerating their deployment in the emerging hydrogen economy.

Bibliography

- [1] Praveen Cheekatamarla. "Hydrogen and the Global Energy Transition—Path to Sustainability and Adoption across All Economic Sectors". In: *Energies* 17.4 (2024). issn: 1996-1073. doi: 10. 3390/en17040807. url: https://www.mdpi.com/1996-1073/17/4/807.
- [2] *Hydrogen : a renewable energy perspective*. International Renewable Energy Agency, 2019, p. 50. isbn: 9789292601515.
- [3] U.S. National Clean Hydrogen Strategy and Roadmap. Tech. rep. 2030.
- [4] Christos M Kalamaras and Angelos M Efstathiou. "Hydrogen Production Technologies: Current State and Future Developments". In: *Conference Papers in Science* 2013.1 (2013), p. 690627. doi: https://doi.org/10.1155/2013/690627. url: https://onlinelibrary.wiley.com/doi/abs/10.1155/2013/690627.
- [5] Alfredo Ursua, Luis M Gandía, and Pablo Sanchis. "Hydrogen Production From Water Electrolysis: Current Status and Future Trends". In: *Proceedings of the IEEE* 100 (Mar. 2012), pp. 410–426. doi: 10.1109/JPROC.2011.2156750.
- [6] Annemieke Berg and Carlos Areán. "Materials for hydrogen storage: Current research trends and perspectives". In: *Chemical communications (Cambridge, England)* 6 (Mar. 2008), pp. 668–681. doi: 10.1039/B712576N.
- [7] Ilaria Lucentini et al. "Review of the Decomposition of Ammonia to Generate Hydrogen". In: Industrial and Engineering Chemistry Research 60.51 (Dec. 2021), pp. 18560–18611. issn: 15205045. doi: 10.1021/acs.iecr.1c00843.
- [8] Julie Ashcroft and Helen Goddin. "Centralised and Localised Hydrogen Generation by Ammonia Decomposition: A technical review of the ammonia cracking process". In: *Johnson Matthey Technology Review* 66.4 (Oct. 2022), pp. 375–385. issn: 20565135. doi: 10.1595/205651322X16554704236047.
- [9] Jinyang Zheng et al. "Development of High Pressure Gaseous Hydrogen Storage Technologies". In: International Journal of Hydrogen Energy 37 (Mar. 2012), pp. 1048–1057. doi: 10.1016/j.ijhydene.2011.02.125.
- [10] Astrid Barona et al. "A Unique Historical Case to Understand the Present Sustainable Development". In: Science and Engineering Ethics 24 (Mar. 2018). doi: 10.1007/s11948-017-9891-5.

- [11] Valentina Cechetto, Luca Di Felice, and Fausto Gallucci. Advances and Perspectives of H2 Production from NH3 Decomposition in Membrane Reactors. Aug. 2023. doi: 10.1021/acs.energyfuels. 3c00760.
- [12] Valentina Cechetto et al. "H2 production via ammonia decomposition in a catalytic membrane reactor". In: *Fuel Processing Technology* 216 (June 2021). issn: 03783820. doi: 10 . 1016 / j . fuproc . 2021 . 106772.
- [13] Stefano Bellini et al. "Mass transport in hydrogen permeation through Pd-based membranes". In: Current Trends and Future Developments on (Bio-) Membranes: Recent Advances in Metallic Membranes. Elsevier, Jan. 2020, pp. 63–90. isbn: 9780128183328. doi: 10.1016/B978-0-12-818332-8.00003-X.
- [14] Valentina Cechetto et al. "Metallic Supported Pd-Ag Membranes for Simultaneous Ammonia Decomposition and H2 Separation in a Membrane Reactor: Experimental Proof of Concept". In: Catalysts 13.6 (June 2023). issn: 20734344. doi: 10.3390/catal13060920.
- [15] J Boon et al. Modelling and systematic experimental investigation of mass transfer in supported palladium-based membrane separators. Tech. rep. 2012.
- [16] WJRVervers et al. "On the modeling of external mass transfer phenomena in Pd-based membrane separations". In: International Journal of Hydrogen Energy 71 (2024), pp. 1121–1133. issn: 0360-3199. doi: https://doi.org/10.1016/j.ijhydene.2024.04.337. url: https://www.sciencedirect.com/science/article/pii/S0360319924016495.
- [17] Jurriaan Boon et al. "Hydrogen permeation through palladium membranes and inhibition by carbon monoxide, carbon dioxide, and steam". In: *Journal of Membrane Science* 496 (Dec. 2015), pp. 344–358. issn: 18733123. doi: 10.1016/j.memsci.2015.08.061.
- [18] Xiangyong Huang et al. "Recent Progress on Hydrogen Production from Ammonia Decomposition: Technical Roadmap and Catalytic Mechanism". In: Molecules 28.13 (2023). issn: 1420-3049. doi: 10.3390/molecules28135245. url: https://www.mdpi.com/1420-3049/28/13/5245.
- [19] David Alique et al. "Review of Supported Pd-Based Membranes Preparation by Electroless Plating for Ultra-Pure Hydrogen Production". In: *Membranes* 8.1 (2018). issn: 2077-0375. doi: 10.3390/membranes8010005. url: https://www.mdpi.com/2077-0375/8/1/5.
- [20] Asuka Suzuki, Hiroshi Yukawa, and Yoshinori Murata. "Consistent description of hydrogen permeation through metal membrane based on hydrogen chemical potential and its application to alloy design". In: *Journal of Materials Research* 32.1 (Jan. 2017), pp. 227–238. issn: 20445326. doi: 10.1557/jmr.2016.416.
- [21] Shigeki Hara et al. "Pressure-Dependent Hydrogen Permeability Extended for Metal Membranes Not Obeying the Square-Root Law". In: *The Journal of Physical Chemistry B* 113.29 (2009), pp. 9795–9801. doi: 10.1021/jp9026767. url: https://doi.org/10.1021/jp9026767.
- [22] Ted Flanagan, D Wang, and Kirk Shanahan. "The role of non-ideality in H permeation through membranes". In: *Scripta Materialia SCRIPTA MATER* 56 (Mar. 2007), pp. 261–263. doi: 10.1016/j.scriptamat.2006.10.029.

- [23] Ververs and Wout. *Palladium-based membranes for dehydrogenation reactions*. Tech. rep. url: www.tue.nl/taverne.
- [24] Maria Nordio et al. "Effect of sweep gas on hydrogen permeation of supported Pd membranes: Experimental and modeling". In: *International Journal of Hydrogen Energy* 44 (Apr. 2019). doi: 10.1016/j.ijhydene.2018.12.137.
- [25] R. J.W. Voncken, I. Roghair, and M. van Sint Annaland. "A numerical study on concentration polarization in 3D cylindrical fluidized beds with vertically immersed membranes". In: *Chemical Engineering Science* 205 (Sept. 2019), pp. 299–318. issn: 00092509. doi: 10.1016/j.ces.2019.05.010.
- [26] Ted B Flanagan and D Wang. "Temperature Dependence of H Permeation through Pd and Pd Alloy Membranes". In: *The Journal of Physical Chemistry A* 116.1 (2012), pp. 185–192. doi: 10.1021/jp2064358. url: https://doi.org/10.1021/jp2064358.
- [27] T A Peters et al. "H2 flux inhibition and stability of Pd-Ag membranes under exposure to trace amounts of NH3". In: Fuel Processing Technology 152 (May 2016). doi: 10.1016/j.fuproc. 2016.06.012.
- [28] S Hara et al. "Hydrogen diffusion coefficient and mobility in palladium as a function of equilibrium pressure evaluated by permeation measurement". In: *Journal of Membrane Science* 421-422 (2012), pp. 355–360. issn: 0376-7388. doi: https://doi.org/10.1016/j.memsci. 2012.08.002. url: https://www.sciencedirect.com/science/article/pii/S0376738812005996.
- [29] Timothy L Ward and Tien Dao. *Model of hydrogen permeation behavior in palladium membranes*. Tech. rep.
- [30] Edward A Mason and Anthony P Malinauskas. "Gas Transport in Porous Media: The Dusty-Gas Model". In: 1983. url: https://api.semanticscholar.org/CorpusID:91199807.
- [31] Jelena Markovic and Radovan Omorjan. "Applicability of linearized Dusty Gas Model for multi-component diffusion of gas mixtures in porous solids". In: *Acta Periodica Technologica* 38 (May 2007). doi: 10.2298/APT0738075M.
- [32] Sandipan Das. "General Dusty Gas Model for porous media with a specified pore size distribution". In: Chemical Engineering Science 203 (May 2019). doi: 10.1016/j.ces.2019.03.085.
- [33] Fernando Roa, Michael J Block, and J.Douglas Way. "The influence of alloy composition on the H2 flux of composite PdCu membranes". In: Desalination 147.1 (2002), pp. 411–416. issn: 0011-9164. doi: https://doi.org/10.1016/S0011-9164(02)00636-7. url: https://www.sciencedirect.com/science/article/pii/S0011916402006367.
- [34] Lianfa Song. "Why is the film model fundamentally wrong but still able to correlate the experimental data in membrane processes?" In: *Journal of Membrane Science* 686 (2023), p. 121987. issn: 0376-7388. doi: https://doi.org/10.1016/j.memsci.2023.121987. url: https://www.sciencedirect.com/science/article/pii/S0376738823006439.

- [35] Andrew L. Zydney. "Stagnant film model for concentration polarization in membrane systems". In: Journal of Membrane Science 130.1 (1997), pp. 275–281. issn: 0376-7388. doi: https://doi.org/10.1016/S0376-7388(97)00006-9. url: https://www.sciencedirect.com/science/article/pii/S0376738897000069.
- [36] Wilko Rohlfs, Gregory P. Thiel, and John H. Lienhard V. "Modeling reverse osmosis element design using superposition and an analogy to convective heat transfer". In: *Journal of Membrane Science* 512 (2016), pp. 38–49. issn: 0376-7388. doi: https://doi.org/10.1016/j.memsci. 2016.03.049. url: https://www.sciencedirect.com/science/article/pii/S0376738816301879.
- [37] Eric Kolor et al. "Advances in Palladium-Based Membrane Research: High-Throughput Techniques and Machine Learning Perspectives". In: *Processes* 12.12 (2024). issn: 2227-9717. doi: 10.3390/pr12122855. url: https://www.mdpi.com/2227-9717/12/12/2855.
- [38] C.Y. Wang et al. "Tube-side mass transfer for hollow fibre membrane contactors operated in the low Graetz range". In: *Journal of Membrane Science* 523 (2017), pp. 235–246. issn: 0376-7388. doi: https://doi.org/10.1016/j.memsci.2016.09.049. url: https://www.sciencedirect.com/science/article/pii/S0376738816305750.
- [39] K C Sandeep et al. "Determination of gas film mass transfer coefficient in a packed bed reactor for the catalytic combustion of hydrogen". In: *Chemical Engineering Science* 202 (2019), pp. 508–518. issn: 0009-2509. doi: https://doi.org/10.1016/j.ces.2019.02.042.url: https://www.sciencedirect.com/science/article/pii/S0009250919302106.
- [40] Bhume Chantaramolee et al. "First principles study of N and H atoms adsorption and NH formation on Pd(111) and Pd3Ag(111) surfaces". In: *Journal of Membrane Science* 474 (2015), pp. 57–63. issn: 0376-7388. doi: https://doi.org/10.1016/j.memsci.2014.09.048. url: https://www.sciencedirect.com/science/article/pii/S0376738814007509.
- [41] Sergey Stolbov and Talat S. Rahman. First Principles Study of Adsorption, Diffusion and Dissociation of NH₃onNiandPdSurfaces. 2005. arXiv: cond-mat/0501060 [cond-mat.mtrl-sci]. url: https://arxiv.org/abs/cond-mat/0501060.
- [42] Didrik R Småbråten, Marie D Strømsheim, and Thijs Peters. "Hydrogen and NH3 co-adsorption on Pd-Ag membranes". In: *International Journal of Hydrogen Energy* 72 (2024), pp. 475–484. issn: 0360-3199. doi: https://doi.org/10.1016/j.ijhydene.2024.05.248. url: https://www.sciencedirect.com/science/article/pii/S0360319924019451.
- [43] Didrik R. Småbråten, Marie D. Strømsheim, and Thijs Peters. "Hydrogen and NH3 co-adsorption on Pd–Ag membranes". In: *International Journal of Hydrogen Energy* 72 (2024), pp. 475–484. issn: 0360-3199. doi: https://doi.org/10.1016/j.ijhydene.2024.05.248. url: https://www.sciencedirect.com/science/article/pii/S0360319924019451.

Appendix A

Property Correlations and Supporting Derivations

A.1 Mixture-Property Relations

The following relations are used for mixture transport properties (referenced in ?? and ??).

A.1.1 Component Viscosity

Sutherland viscosity law. Component viscosities are calculated using Sutherland's law:

$$\mu_i(T) = \mu_{i,\text{ref}} \left(\frac{T}{T_{\text{ref}}}\right)^{\frac{3}{2}} \frac{T_{\text{ref}} + S_i}{T + S_i},\tag{A.1}$$

where $\mu_{i,\text{ref}}$ is the reference viscosity, T_{ref} is the reference temperature, and S_i is the Sutherland constant for component i.

A.1.2 Mixture Viscosity

Wilke's mixing rule. Given component viscosities μ_i and mole fractions y_i , the mixture viscosity is:

$$\mu_{\text{mix}} = \sum_{i} \frac{y_i \mu_i}{\sum_{j} y_j \phi_{ij}},\tag{A.2}$$

$$\phi_{ij} = \frac{1}{\sqrt{8}} \left(1 + \frac{M_j}{M_i} \right)^{-\frac{1}{2}} \left[1 + \left(\frac{\mu_i}{\mu_j} \right)^{1/2} \left(\frac{M_j}{M_i} \right)^{1/4} \right]^2, \tag{A.3}$$

where M_i and M_j are the molecular weights of components i and j, respectively.

A.1.3 Binary Diffusion Coefficients

Fuller-Schettler-Giddings correlation. Binary diffusion coefficients are calculated as:

$$D_{AB} = 10^{-4} \frac{0.001 \, T^{1.75} \sqrt{\frac{1}{M_A} + \frac{1}{M_B}}}{P\left[(V_A)^{1/3} + (V_B)^{1/3} \right]^2} \quad (\text{m}^2/\text{s}), \tag{A.4}$$

where T is the temperature (K), M_A and M_B are the molecular weights (g/mol), P is the pressure (Pa), and V_A , V_B are the molecular diffusion volumes (cm³/mol).

A.1.4 Effective Mixture Diffusivity

For multicomponent systems, the effective diffusivity of species i in the mixture is given by:

$$\frac{1-y_i}{D_{i,\text{mix}}} = \sum_{j \neq i} \frac{y_j}{D_{ij}},\tag{A.5}$$

where y_i is the mole fraction of species i and D_{ij} are the binary diffusion coefficients.

A.1.5 Viscosity Coefficients

Table A.1: Viscosity correlation coefficients for individual species.

Species	C_1	C_2	C_3	C_4
H_2	1.797×10^{-7}	0.6850	-0.59	140
N_2	6.5592×10^{-7}	0.6081	54.714	0
NH_3	4.1855×10^{-6}	0.9806	30.8	0

A.1.6 Component Properties

Table A.2: Component properties used in transport property correlations.

Component	M_i (kg/mol)	V_i (cm ³ /mol)	$\mu_{i, ext{ref}}$ (Pa·s)	$T_{ m ref}$ (K)	<i>S_i</i> (K)
H_2	2.016×10^{-3}	7.07	8.76×10^{-6}	293.85	72.0
N_2	28.01×10^{-3}	17.9	1.781×10^{-5}	300.55	111.0
NH_3	17.031×10^{-3}	14.9	9.82×10^{-6}	300.00	370.0

These values are substituted into the following standard transport property correlations:

- Sutherland viscosity law: see Equation A.1.
- Fuller-Schettler-Giddings binary diffusivity: see Equation A.4.
- Wilke's mixing rule for mixture viscosity: see Equation A.2-Equation A.3.

Note: NH_3 viscosity parameters are estimated using proxy values due to limited high-ter availability.	nperature data
A Multi-Physics Model of Hydrogen Permeation through Pd-Ag Membranes	53



Appendix B

Dusty Gas Model Equations

B.1 General Form with Viscous Contribution

$$\sum_{\substack{j=1\\i\neq i}}^{n} \frac{x_i N_j - x_j N_i}{p D_{i,j}^{\text{eff}}} - \frac{N_i}{p D_{i,K}^{\text{eff}}} = \frac{1}{RT} \frac{\partial x_i}{\partial r} + \frac{x_i}{pRT} \left(\frac{B_0 p}{\mu D_{i,K}^{\text{eff}}} + 1 \right) \frac{\partial p}{\partial r}$$
(B.1)

B.2 Negligible Pressure Drop (No Viscous Contribution)

$$\sum_{\substack{j=1\\j\neq i}}^{n} \frac{x_i N_j - x_j N_i}{p D_{i,j}^{\text{eff}}} - \frac{N_i}{p D_{i,K}^{\text{eff}}} = \frac{1}{RT} \frac{\partial x_i}{\partial r}$$
(B.2)

B.3 Rewritten Form

With y = mole fraction, x = coordinate:

$$\frac{\partial y_i}{\partial x} = \sum_{\substack{j=1\\i \neq j}}^n \frac{y_i N_j - y_j N_i}{c_{\text{tot}} D_{i,j}^{\text{eff}}} - \frac{N_i}{c_{\text{tot}} D_{i,K}^{\text{eff}}}$$
(B.3)

B.4 Three-Component System

$$\frac{\partial y_1}{\partial x} = \frac{y_1 N_2 - y_2 N_1}{c_{\rm tot} D_{1,2}^{\rm eff}} + \frac{y_1 N_3 - y_3 N_1}{c_{\rm tot} D_{1,3}^{\rm eff}} - \frac{N_1}{c_{\rm tot} D_{1,K}^{\rm eff}} \tag{B.4}$$

$$\frac{\partial y_2}{\partial x} = \frac{y_2 N_3 - y_3 N_2}{c_{\text{tot}} D_{23}^{\text{eff}}} + \frac{y_2 N_1 - y_1 N_2}{c_{\text{tot}} D_{21}^{\text{eff}}} - \frac{N_2}{c_{\text{tot}} D_{2K}^{\text{eff}}}$$
(B.5)

$$\frac{\partial y_3}{\partial x} = \frac{y_3 N_1 - y_1 N_3}{c_{\rm tot} D_{3,1}^{\rm eff}} + \frac{y_3 N_2 - y_2 N_3}{c_{\rm tot} D_{3,2}^{\rm eff}} - \frac{N_3}{c_{\rm tot} D_{3,K}^{\rm eff}} \tag{B.6}$$

B.5 Two-Component Dusty Gas Model

$$-\frac{1}{RT}\frac{dP_2}{dz} = \frac{1}{D_{K2}} \left[N_2 + x_2 B_0 \frac{P}{\mu RT} \frac{dP}{dz} \right] + \frac{x_1 N_2 - x_2 N_1}{D_{12}}$$
(B.7)

$$-\frac{1}{RT}\frac{dP_1}{dz} = \frac{1}{D_{K1}} \left[N_1 + x_1 B_0 \frac{P}{\mu RT} \frac{dP}{dz} \right] + \frac{x_2 N_1 - x_1 N_2}{D_{12}} \tag{B.8}$$

Flux relation:

$$N_{1} = -\frac{D_{K1}}{RT} \left(1 + \frac{B_{0}P}{\mu D_{KA}} \right) \frac{dP}{dz}$$
 (B.9)

Pressure derivative relation:

$$\frac{dP_2}{dz} = x_2 \frac{dP}{dz} + P \frac{dx_2}{dz} \tag{B.10}$$

B.6 Simplified Expressions

$$-P\frac{dx_2}{dz} = \frac{1}{D_{K2}}x_2B_0\frac{P}{\mu}\frac{dP}{dz} + \frac{x_2}{D_{12}}D_{K1}\frac{B_0P}{\mu D_{KA}}\frac{dP}{dz} + \frac{x_2}{D_{12}}D_{K1}\frac{dP}{dz} + x_2\frac{dP}{dz}$$
(B.11)

B.7 Flux Expression

$$N_1 = \frac{D_{K1}}{RT} \left(\left(\frac{x_1}{D_{K1}} + \frac{x_2}{D_{K2}} \right) \frac{PB_0}{\mu} + 1 \right) \frac{dP}{dz}$$
 (B.12)

B.8 Relation

$$\frac{x_1}{D_{K1}} + \frac{x_2}{D_{K2}} = \frac{1}{D_{KA}} \tag{B.13}$$

B.9 One-Component Dusty Gas Model

$$-\frac{\mathsf{flux}}{D} = \frac{1}{RT} \left(\frac{B_0 p}{\mu D} + 1 \right) \frac{\partial p}{\partial r} \tag{B.14}$$

$$\frac{\partial p}{\partial r} = \frac{-RT \cdot \text{flux}}{\left(\frac{B_0 p}{\mu} + D\right)}$$
(B.15)

B.10 Parameter Definitions

$$B_0 = \frac{\varepsilon}{\tau} \frac{d_p^2}{32} \tag{B.16}$$

$$D = \frac{\varepsilon}{\tau} \frac{d_p}{3} \sqrt{\frac{8RT}{\pi M_i}}$$
 (B.17)

Appendix C

Experimental Permeation Data

C.1 Experimental Permeation Data

This appendix presents the complete experimental dataset for hydrogen permeation through Pd-Ag membranes in both H_2/N_2 and H_2/NH_3 systems. All experiments were conducted at a constant feed flow rate of 2.0 L min⁻¹ (STP).

C.1.1 H_2/N_2 System

Table C.1: Experimental hydrogen permeation data for H₂/N₂ mixtures

Temperature (°C)	Feed Pressure (bar _g)	H ₂ Mole Fraction (-)	Permeate Flow (mL min $^{-1}$)	H ₂ Recovery Fraction (-)
400	2	0.95	1621.3	0.853
400	2	0.90	1381.3	0.767
400	2	0.85	1194.0	0.702
400	1	0.95	1165.8	0.614
400	1	0.90	954.3	0.530
400	1	0.85	791.0	0.465
425	2	0.95	1672.0	0.880
425	2	0.90	1445.7	0.803
425	2	0.85	1252.8	0.737
425	1	0.95	1316.8	0.693
425	1	0.90	1065.8	0.592
425	1	0.85	791.0	0.465
450	2	0.95	1715.9	0.903
450	2	0.90	1495.3	0.831
450	2	0.85	1287.0	0.757
450	1	0.95	1469.6	0.773
450	1	0.90	1201.2	0.667
450	1	0.85	977.8	0.575

C.1.2 H_2/NH_3 System

Table C.2: Experimental hydrogen permeation data for H₂/NH₃ mixtures

Temperature (°C)	Feed Pressure (bar $_{g}$)	H ₂ Mole Fraction (-)	Permeate Flow $(mL min^{-1})$	\mathbf{H}_2 Recovery Fraction (-)
400	2	0.95	1529.8	0.805
400	2	0.90	1283.6	0.713
400	2	0.85	1081.4	0.636
400	1	0.95	1113.8	0.586
400	1	0.90	874.1	0.486
425	2	0.95	1556.3	0.819
425	2	0.90	1324.2	0.736
425	2	0.85	1135.1	0.668
425	1	0.95	1478.8	0.778
425	1	0.90	930.4	0.517
425	1	0.85	754.9	0.444
450	2	0.95	1736.4	0.914
450	2	0.90	1509.7	0.839
450	2	0.85	1300.7	0.765
450	1	0.95	1478.8	0.778
450	1	0.90	1181.5	0.656
450	1	0.85	952.9	0.561

C.1.3 Experimental Conditions

The experimental conditions for all measurements were:

• Feed flow rate: $2.0 L min^{-1}$ (STP)

• Temperature range: 400-450°C

• Feed pressure: 1–2 bar_g (gauge pressure)

• H₂ mole fractions: 0.85, 0.90, 0.95

• Membrane: Pd-Ag composite membrane

All permeate flow rates are reported at standard temperature and pressure (STP: 273.15 K, 1 atm). The hydrogen recovery fraction (HRF) is defined as the ratio of hydrogen permeated to hydrogen fed to the system.

*Disclaimer: Tools like ChatGPT and Grammarly have been used to check grammar mistakes, improve the academic style, and readability of the text.